Correspondence to:
Y. Tal,
yuvtal@bgu.ac.il

Dynamics and Near-Field Surface Motions of Transitioned Supershear Laboratory Earthquakes in Thrust Faults

Yuval Tal[1,2] , **Vito Rubino[3]** , **Ares J. Rosakis[3]** , **and Nadia Lapusta[2,4]**

[1]Department of Earth and Environmental Sciences, Ben-Gurion University of the Negev, Beer Sheva, Israel, [2]Seismological Laboratory, Division of Geological and Planetary Sciences, California Institute of Technology, Pasadena, CA, USA, [3]Graduate Aerospace Laboratories, California Institute of Technology, Pasadena, CA, USA, [4]Division of Engineering and Applied Science, California Institute of Technology, Pasadena, CA, USA

Abstract We study how the asymmetric geometry of thrust faults affects the dynamics of supershear ruptures and their associated trailing Rayleigh ruptures as they interact with the free surface, and investigate the resulting near-field ground motions. Earthquakes are mimicked by propagating laboratory ruptures along a frictional interface with a 61° dip angle. Using an experimental technique that combines ultrahigh-speed photography with digital image correlation, we produce sequences of full-field evolving measurements of particle displacements and velocities. Our full-field measurement capability allows us to confirm and quantify the asymmetry between the experimental motions of the hanging and footwalls, with larger velocity magnitudes occurring at the hanging wall. Interestingly, because the motion of the hanging wall is generally near-vertical, while that of the footwall is at dip direction shallower than the dip angle of the fault, the horizontal surface velocity components are found to be larger at the footwall than at the hanging wall. The attenuation in surface velocity with distance from the fault trace is generally larger at the hanging wall than at the footwall and it is more pronounced in the vertical component than in the horizontal one. Measurements of the rotations in surface motions confirm experimentally that the interaction of the rupture with the free surface can be interpreted through a torqueing mechanism that leads to reduction in normal stress near the free surface for thrust earthquakes. Nondimensional analysis shows that the experimental measurements are consistent with larger-scale numerical simulations as well as field observations from thrust earthquakes.

Plain Language Summary The asymmetric interaction of thrust earthquakes with the Earth's surface leads to complex dynamic behavior and strongly asymmetric ground motions. Near-fault measurements from such earthquakes are rare and do not allow for detailed characterization of the earthquake rupture and the associated near-field ground motions. In this study, we create controlled ruptures in a laboratory set-up mimicking the thrust fault earthquake process. We utilize a unique, optical, ultrahigh-speed imaging technique to observe such updip laboratory earthquakes at high spatial resolution and in real time, and to analyze their complex dynamic interactions with the free surface. Such a study would be difficult to achieve in the field because of the typical spatial sparsity of the recorded data. The experiments allow us to quantify the differences in ground motion between the two sides of the fault, the decrease of ground motion with distance from the fault, and the dynamic surface rotations. Moreover, the experimental observations enable us to directly relate the measured near-field ground motion to the state of the earthquake rupture on the fault.

1. Introduction

The asymmetric geometry of thrust faults with respect to the Earth's surface leads to complex dynamic behavior of updip ruptures and amplification of ground motions, with asymmetry between the hanging wall and footwall. Seismological observations have generally showed larger ground motions at the hanging wall for both blind and surface-rupturing thrust earthquakes. The larger motions were attributed to the closer proximity of hanging wall seismic stations to the fault (Abrahamson & Somerville, 1996) and to waves trapped in the hanging wall (Brune, 1996; Nason, 1973). Larger peak ground accelerations at the hanging wall were observed for the 1971 Mw 6.6 San Fernando (Allen et al., 1998; Nason, 1973; Steinbrugge et al., 1975), the 1994 Mw 6.7 Northridge (Abrahamson & Somerville, 1996), and the 1999 Mw 7.7 Chi-Chi (Chang et al., 2004; Shin & Teng, 2001) earthquakes. For the 2008 Mw 7.9 Wenchuan earthquake, the hanging-wall effect was observed for the peak ground accelerations at periods below 1.0 s, but was absent at larger periods or for the peak ground velocities (Li et al., 2010; Liu & Li, 2009). Zhang et al. (2019) observed the hanging-wall effects for both the vertical

and horizontal components, but with the former significantly more prominent than the latter. The 2013 Mw 6.6 Lushan earthquake also showed the hanging-wall effect only for short periods (Bai, 2017). Because near-fault observations from thrust earthquakes are limited to few earthquakes, they cannot fully constrain the geometrical effect of thrust fault on the ground motions (Donahue & Abrahamson, 2014). Moreover, seismic observations may be affected by the other factors, such as the lithology and topography.

Numerical studies of thrust earthquakes (Duan & Oglesby, 2005; Ma & Beroza, 2008; Oglesby & Day, 2001; Oglesby et al., 1998, 2000; Scala et al., 2019; Shi et al., 1998; Yin & Denolle, 2021) also showed larger ground motion at the hanging wall than at the footwall, with the amplification at hanging wall increasing as the dip angle of the fault decreases (Oglesby et al., 1998). Simulations of multiple earthquake cycles on thrust fault with dip angle of 45° (Duan & Oglesby, 2005) revealed the occurrence of a dominant vertical component of ground motion at the hanging wall, but a dominant horizontal component at the footwall. Several numerical and theoretical studies showed that the interaction of the thrust ruptures with the free surface results in a time-dependent fault-normal traction (Aldam et al., 2016; Kozdon & Dunham, 2013; Ma & Beroza, 2008; Madariaga, 2003; Nielsen, 1998; Oglesby et al., 1998, 2000), in which the normal traction increases ahead of the rupture front and decreases behind it. Because changes in the normal traction affect the frictional shear resistance, its decrease can lead to larger slip and slip rate on the fault and amplification the ground motion (Oglesby et al., 1998).

Brune (1996) performed laboratory experiments on a foam-rubber model with thrust wedge geometry of dip angle of 25° and showed that, in the presence of large deformations, the interaction of the rupture with the free surface leads to significant fault opening near the free surface that traps the energy at the hanging wall. Foam rubber, however, is not a linear elastic and brittle material and it is not an optimal analogue material for the rocks in the upper crust. Furthermore, the ruptures in those experiments already developed initial opening near the growing shear rupture tip, well before arriving at the free surface, a phenomenon which is clearly an indication of large deformations. Hence, the foam-rubber results did not conclusively resolve the issue of whether fault opening is feasible and whether this phenomenon is not merely an artifact of the large-deformation, non-linear elastic behavior of foam rubber, which is not exhibited by brittle rocks.

Using photoelastic images and highly resolved discrete laser-velocimetry measurements from dynamic ruptures experiments on brittle Homalite specimens with a pre-existing fault at a dip angle of 61° under uniaxial compressive loading of 2.5 MPa, Gabuchian et al. (2017) confirmed that even within the linear, small deformation, regime typical of natural faults, classical sub-Raleigh thrust ruptures may open the faults near the free surface. For super-shear ruptures, their results indicated that the opening, although present, was not as pronounced. Based on complementary numerical simulations, they suggested that the opening and decrease of normal traction are the results of a geometrically induced torque mechanism (Madariaga, 2003), in which the hanging-wall wedge undergoes pronounced rotation in one direction as the earthquake rupture approaches the free surface, then, as rupture breaks the free surface, the torque is released with unclamping of the hanging-wall near the free surface. Moreover, they suggested that this mechanism can explain the large shallow slip observed for the 2011 Mw 9.0 Tohoku earthquake in Japan and the 1999 Mw 7.7 Chi-Chi earthquake in Taiwan (Fujiwara et al., 2011; Lay et al., 2011; Ma et al., 2001), despite the existence of frictionally stable sediments at shallow depth (e.g., Saffer & Marone, 2003), as demonstrated in numerical models (Kozdon & Dunham, 2013).

In an earlier study using dynamic photoelasticity and laser velocimetry, Gabuchian et al. (2014) quantitatively explored the dynamics of vertical ground motions with a similar experimental configuration, but with the laser velocimeters located at discreet points along the free surface. They also highlighted the substantial differences in ground motion behavior resulting when either sub-Rayleigh or super-shear ruptures, travelling updip, reach the free surface. Similar to the seismological observations and numerical simulations, these early experimental surface-normal motions verified in detail the substantial asymmetry between the hanging wall and the footwall, with larger velocity amplitudes for the hanging wall. The experimental results also highlighted the need for quantitative full-field measurements in order to explore this complex phenomenon in detail and at different rupture-speed regimes.

Tal et al. (2020) analyzed the evolution of fault-normal traction and frictional resistance response during the interaction of laboratory thrust ruptures with the free surface in an experimental configuration similar to that of Gabuchian et al. (2014, 2017), but with a new full-field imaging technique, which combines ultra-high speed photography and digital image correlation (DIC; Rosakis et al., 2020; Rubino et al., 2017, 2019, 2020; Tal et al., 2019).

Similarly to the numerical simulations of Ma and Beroza (2008), Nielsen (1998), and Oglesby et al. (1998, 2000), significant reductions in normal stress were observed during the interaction of the experimental ruptures with the free surface. Moreover, a temporary complete release of normal traction was observed for experiments under the initial compressive stresses of less than 7.4 MPa, which is consistent with the opening measured by the nodal velocimeters in the experiments of Gabuchian et al. (2017). In contrast to standard friction formulation often used in numerical simulations, the experiments also showed a significant delay in the response of frictional shear resistance to the variation in normal traction, consistent with some earlier studies (Linker & Dieterich, 1992; Prakash & Clifton, 1993), which might decrease the effect of normal traction reductions on the rupture process.

In this study, we use the same experimental set up and imaging technique as in Tal et al. (2020), but focus on dynamics of thrust ruptures as they interact with the free surface and the effect of the free surface on the near-fault ground motion. The original version of this set-up (Gabuchian et al., 2014) used dynamic photoelasticity to qualitatively visualize the rupture process and particle velocimeters to record the resulting ground motion at a few discrete locations at the free surface. The coupled ultrahigh-speed photography and DIC method used in this study allows us to produce full-field maps of displacement and particle-velocity histories of the ruptures as they interact with the free surface at time intervals of 1 μs. This versatile technique provides measurements of both the horizontal and vertical components of surface velocities and displacements, which enables us to study the differences in ground motion between the hanging and footwall, the attenuation of surface velocities with distance from the fault in the near field, and the relationship between the near-field ground motions and the rupture on the fault. In addition, measurements of the rotations of velocities and displacements during the interactions of the rupture with the free surface allow us to examine experimentally the geometrically induced torque mechanism suggested earlier (e.g., Gabuchian et al., 2017; Madariaga, 2003).

The experimental ruptures in this study are supershear when they reach the free surface. The physical existence of supershear, mode-II, cracks and frictional ruptures propagating along weekly bonded or frictional interfaces (faults), previously considered to be a theoretical possibility (Burridge, 1973; Freund, 1979), was first demonstrated experimentally through optical experiments of the dynamic shear rupture process (Rosakis, 2002; Rosakis et al., 1999; Xia et al., 2004) of the type presented here. "Super-shear" (more precisely, "intersonic") cracks or ruptures are defined as dynamic ruptures whose speeds have exceeded the shear wave speed but is still below the pressure wave speed of the surrounding solid. Such ruptures may sometimes be born intersonic or in other cases, they may initially grow with a sub-Rayleigh rupture speed and then transition to supershear speeds. The mechanics of sub-Rayleigh to supershear rupture transition has been studied both theoretically (Andrews, 1976; Dunham & Archuleta, 2004; Liu & Lapusta, 2008) and experimentally (Mello et al., 2016; Rosakis et al., 2007; Xia et al., 2004) but it is still an active subject of research in geophysics. In the context of the present study, considering transitioned supershear ruptures enables us to carefully investigate the interaction of both the supershear front and the associated trailing Rayleigh rupture (a rupture trailing the supershear rupture tip which is generated following the speed transition) with the free surface, and the differences between them. Such a comparison is especially valuable since it is uncertain whether thrust earthquakes are mostly sub-Rayleigh or supershear as they approach the free surface due to limitations in density of field measurements and inversion techniques.

2. Monitoring the Dynamics of Thrust-Fault Laboratory Earthquakes

2.1. Laboratory Earthquake Setup and Ultrahigh-Speed Diagnostics

Thrust earthquakes are modeled by dynamic ruptures propagating along a preexisting interface (experimental fault) with a dip angle of $\beta = 61°$ between two Homalite-100 quadrilateral plates (sample dimensions of 25×18 cm; Figure 1). The plates are loaded under uniaxial compression P, resulting in the initial shear and normal stresses on the fault of $\tau_0 = P\sin(61°)\cos(61°)$ and $\sigma_0 = P\sin^2(61°)$, respectively. The experimental apparatus is described more in detail in our prior work (Rubino et al., 2017, 2019; Tal et al., 2020). In this paper, we report the results of four experiments with $P = 4.9$, 7.4, 10, and 15.1 MPa. In all experiments, the interfaces are first polished to remove machining defects, and then bead-blasted with microbeads of 104–211 μm to introduce a reproducible roughness (Lu et al., 2010; Mello et al., 2010; Rubino et al., 2019). The ruptures are nucleated at a distance of $x_f = 11.5$ cm from the free surface by a local pressure release provided by the expansion of a NiCr wire due to an electrical discharge (2 kV) of a high-voltage capacitor (Cordin 640), where x_f is the distance along the fault. Once nucleated, the ruptures propagate spontaneously, driven by the far-field stresses τ_0 and σ_0. With $\beta = 61°$, the ratio of shear to normal stress on the fault enables to load the plates to the desired initial stress without sliding and to
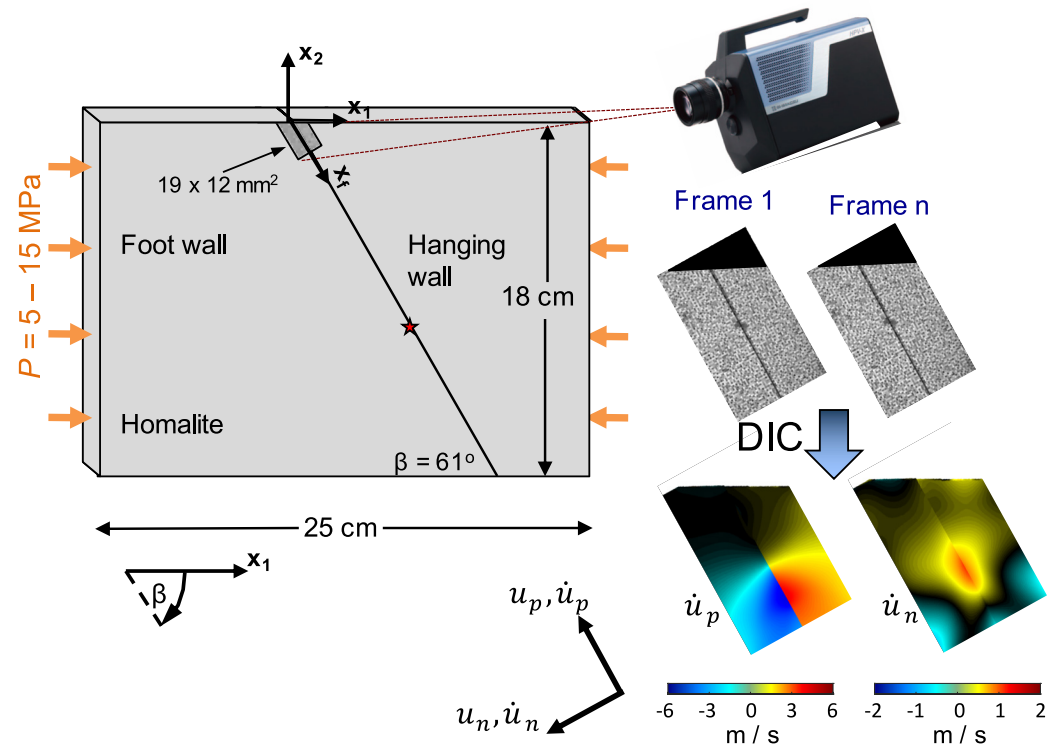
Figure 1. Experimental setup. Dynamic shear ruptures are initiated by a small burst of a NiCr wire at distance $x_f = 11.5$ cm from the free surface and propagate spontaneously along a frictional interface inclined at a dip angle $\beta = 61°$ between two Homalite plates, which are loaded under a compressional load P. An ultrahigh-speed camera system (Shimadzu HPV-X) and a high-speed white light source system (Cordin 605) are used to record 128 images of a target area of 19×12 mm^2 near the free surface at a rate of 1 million frames/second. The images are analyzed with the digital image correlation method to obtain full-field displacement and velocity fields.

obtain intensive ruptures. The low shear modulus of Homalite ($\mu = 1.96$ GPa) enables to produce well-developed dynamic ruptures in samples of tens of centimeters. Homalite-100 is a highly strain-rate-sensitive material (Singh & Parameswaran, 2003), and the local high-strain-rate wave speeds control the rupture speed (Gori et al., 2018; Rubino et al., 2019). The shear and pressure wave speeds for Homalite-100 are $c_s = 1.28$ km/s and $c_p = 2.6$ km/s (Mello et al., 2010), respectively, and the Rayleigh wave speed is $c_R = 0.92c_s = 1.18$ km/s.

In order to obtain full-field measurements of the deformation associated with the ruptures, a target area (19×12 mm^2) coated with a random black-dots pattern is monitored near the free surface using an ultrahigh-speed camera system (Shimadzu HPV-X) and a high-speed light system (Cordin 605). The camera records a sequence of 128 images of the patterns distorted by the propagating rupture with a resolution of 400×250 pixels^2, at temporal sampling of 1 million frames/second and exposure time of 200 ns. To minimize optical aberrations, we employ a fixed focal distance telephoto lens (Nikon Micro-Nikkor 200 mm f/4D IF-ED).

2.2. Full-Field Analysis of Thrust-Fault Ruptures With the Digital Image Correlation Method

Similarly to Rubino et al. (2017, 2019, 2020), we use the local DIC software Vic-2D (Correlation Solutions Inc.) to produce evolving maps of displacements parallel (u_p) and normal (u_n) to the fault from the sequence of images acquired with the ultrahigh-speed camera. In local DIC methods, displacements are calculated by using pattern matching algorithms over image subsets, separated by a distance, referred to as step. In this study, the correlation is performed separately for the domains above and below the fault employing image subsets of 41×41 pixels^2 that are overlapped with a step of 1 pixel. While standard local DIC techniques provide the displacement map up to half a subset away from the boundaries, Vic-2D extrapolates the displacements up to the fault. We use a non-local filter (Buades et al., 2006, 2008; Rubino et al., 2015) to remove the high-frequency noise from the displacement fields, then a self-developed post-processing algorithm (Tal et al., 2019) that locally adjusts the
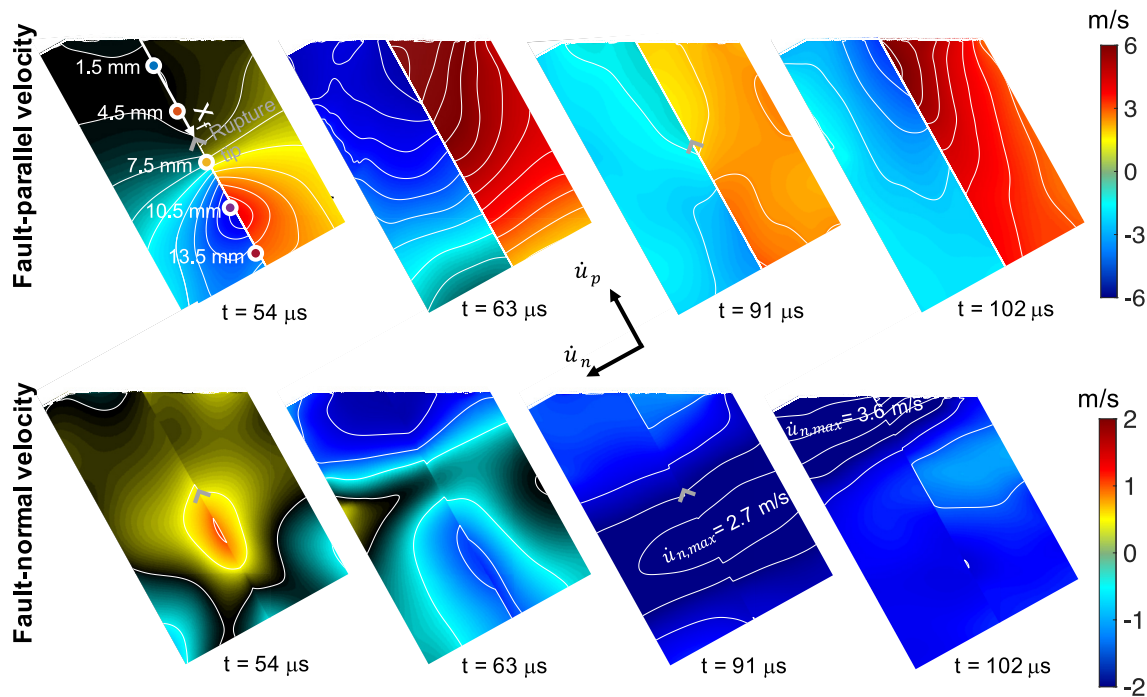
Figure 2. Snapshots of full-field fault-parallel (top panels) and fault-normal velocities (bottom panels) at the following stages of Exp #1 ($P = 15$ MPa): Propagation of the supershear rupture through the field of view (FOV) ($t = 54$ μs), interaction of the supershear rupture with the free surface ($t = 63$ μs), propagation of the trailing Rayleigh rupture through the FOV ($t = 91$ ms), and interaction of the trailing Rayleigh with the free surface ($t = 102$ ms). The location of the rupture tip in the images where the ruptures propagate through the field of view is marked by a gray arrowhead. The velocity field of the supershear rupture shows dominant fault-parallel motion, while that of the trailing Rayleigh shows dominant fault-normal motion.

displacements near the fault to ensure continuity of tractions across the fault. Ensuring traction continuity across the fault is a key feature in the analysis of dynamic ruptures approaching the free surface, as small deviations in the displacement measurements due to noise would result in unphysical tractions. Our post-processing procedure (Tal et al., 2019) allowed capturing rapid normal stress variations across the interface (Tal et al., 2020) due to the interaction of dynamic shear ruptures with the free surface.

The fault-parallel velocity ($\dot{u}_p$) and fault-normal velocity ($\dot{u}_n$) are computed from the sequence of the displacement components u_p and u_n, respectively, using a central-difference scheme. The slip δ is computed as the difference between the fault-parallel velocity just above and below the fault, and the slip rate, $\dot{\delta}$, is its time derivative. To discuss the ground motions, the velocity and displacement fields are also rotated from the coordinate system (x_p, x_n) with axes parallel and normal to the fault into a coordinate system (x_1, x_2) that is parallel and normal to the free surface (Figure 1). We estimate the rupture speed V_r in the experiments by tracking the rupture tip as it propagates across the field of view (FOV). We compute the rupture arrival time at each location along the fault as the time in which $\dot{\delta}$ initially exceeds a threshold value of $\dot{\delta}_{thr} = 0.5$ m/s. Because this time may not coincide with an actual data point, a linear interpolation is performed between frames right before and after exceeding $\dot{\delta}_{thr}$. We smooth the curve of the rupture tip position versus time with a Butterworth filter and estimate V_r from the average slope of the curve.

3. Experimental Results of Laboratory Thrust Earthquakes

3.1. Dynamic Rupture Behavior During Interaction With the Free Surface

Before analyzing the ground motions, we start by exploring the full-field behavior of the dynamic ruptures as they approach and interact with the free surface. A series of full-field images of the fault-parallel and fault-normal velocities near the free surface is shown in Figure 2 during Exp. #1 performed under the largest compressive load of $P = 15.1$ MPa. The experimental conditions generate a supershear rupture, propagating through the FOV at a rupture speed of $V_r = 2.09$ km/s $= 1.63 c_s$. As the rupture propagates through the FOV ($t = 54$ μs after nucleation),

$\dot{u}_p$ shows an antisymmetric pattern, in which the hanging wall slides upward and the footwall slides downward, both with maximum values of ~3 m/s on the fault, at a location 5 mm behind the rupture tip. At this stage, both sides of the fault show a positive normal movement (toward the footwall), with maximum values of $\dot{u}_n \sim 0.8$ m/s at the same location. A more detailed description of the features associated with propagating supershear and sub Rayleigh ruptures, away from the free surface, is given by Rubino et al. (2020). As the rupture reaches the free surface ($t = 63$ μs), there is a significant increase in $\dot{u}_p$ and $\dot{u}_n$, as well as a change in direction of $\dot{u}_n$ into mostly negative normal movement. The supershear rupture is followed by another rupture, traveling at the speed of the Rayleigh wave. This disturbance is what remains from the initial rupture that gave rise to the supershear one (Xia et al., 2004), and subsequently trails behind it as documented by previous experimental measurements (Gabuchian et al., 2014; Mello et al., 2010, 2016; Rosakis et al., 2007; Rubino et al., 2020). The propagation of the trailing-Rayleigh rupture through the FOV ($t = 91$ μs) is mostly observed in the $\dot{u}_n$ component (as is characteristic of all sub-Rayleigh ruptures), which shows an elongated feature of $\dot{u}_n < -2.5$ m/s (large rightward movement) perpendicular to the fault. The observation of such a trailing Rayleigh rupture indicates that a transition from a sub-Rayleigh to supershear rupture had occurred (Andrews, 1976; Burridge, 1973; Lu et al., 2010; Rosakis et al., 2007; Xia et al., 2004). When the trailing-Rayleigh rupture arrives at the free surface ($t = 102$ μs), both $\dot{u}_p$ and $\dot{u}_n$ increase (in absolute value). Assuming a constant propagation speed of the rupture at each regime and that the rupture propagated at the Rayleigh wave speed before the transition to supershear, we can estimate the sub-Rayleigh to supershear transition distance, L_{trans}, with the following expression (Rubino et al., 2020):

$$L_{\text{trans}} = c_R \frac{(x_d - t_d V_r)}{(c_R - V_r)}, \tag{1}$$

where t_d is arrival time of the rupture at a given distance x_d from the nucleation site. The estimated rupture speed of $V_r = 2.09$ km/s in Exp. #1 indicates that the rupture transitioned to supershear at a small transition distance of $L_{\text{trans}} = 5.6$ mm from the nucleation site.

Plots of the time histories of slip rate, $\dot{\delta}$, at different locations along the fault (Figure 3a) provide further insight into the effect of the free surface on the rupture process itself. At the largest distance from the free surface ($x_f = 13.5$ mm), there are two separated peaks in $\dot{\delta}$ that correspond to the arrival ($\dot{\delta} = 6.5$ m/s at $t = 54$ μs) and reflection ($\dot{\delta} = 9$ m/s at $t = 69$ μs) of the supershear rupture. As the distance to the free surface decreases, the peaks of arrival and reflection merge together, with a transition into a single peak of $\dot{\delta} = 12.5$ m/s near the free surface ($x_f = 1.5$ mm). The trailing-Rayleigh rupture shows a clear peak of $\dot{\delta} = 9.5$ m/s at $x_f = 1.5$ mm, but as x_f increases, the peak becomes smaller and wider, with a weak signal at $x_f = 13.5$ mm.

Experiments under lower compressive loads are characterized by weaker ruptures with smaller slip rates. The ruptures show similar characteristics to those described above, featuring a supershear rupture in the front followed by a trailing Rayleigh rupture. However, as P decreases, there is a transition from a dominant supershear rupture to a dominant trailing Rayleigh rupture. In Exp. #4, which was conducted under the lowest compressive load of $P = 4.9$ MPa (Figure 3b), the peak slip rate of the supershear rupture near the free surface ($x_f = 1.5$ mm) is $\dot{\delta} = 2.8$ m/s, while that of the trailing Rayleigh is $\dot{\delta} = 5$ m/s. Moreover, there is a delay of ~5 μs in the arrival of the supershear rupture to FOV compared to Exp. #1 because of a slightly slower rupture speed of $V_r = 2$ km/s $= 1.57 c_s$ and a larger transition distance of $L_{\text{trans}} = 12.8$ mm.

3.2. Experimental Measurements of the Ground Motion

3.2.1. Supershear Rupture Front

Snapshots of the of full-field particle velocity magnitude, $|\dot{\mathbf{u}}|$, with overlaid velocity vectors on the fault and on the free surface, during different stages of Exp. #1 (Figure 4), shed light on the dynamics of the supershear rupture and the subsequent trailing Rayleigh rupture during the interaction with the free surface, as well as their effects on the ground motion. The supershear rupture (Figure 4, top panels) approaches the free surface ($t = 57$ μs) with a peak particle velocity magnitude of 4 m/s and transition from a dominant fault-normal particle motion ahead of the rupture front to a fault-parallel particle motion behind it. Correspondingly, at the surface, the right part of the hanging wall, which is already behind the rupture front, moves parallel to the fault with a velocity magnitude of $|\dot{\mathbf{u}}|_s = 2$ m/s. The surface velocities, $\dot{\mathbf{u}}_s$, decrease and rotate in locations on the surface that are ahead the rupture front (decreasing x_1). During the interaction of the rupture with the free surface ($t = 63$ μs), $|\dot{\mathbf{u}}|$ increases and
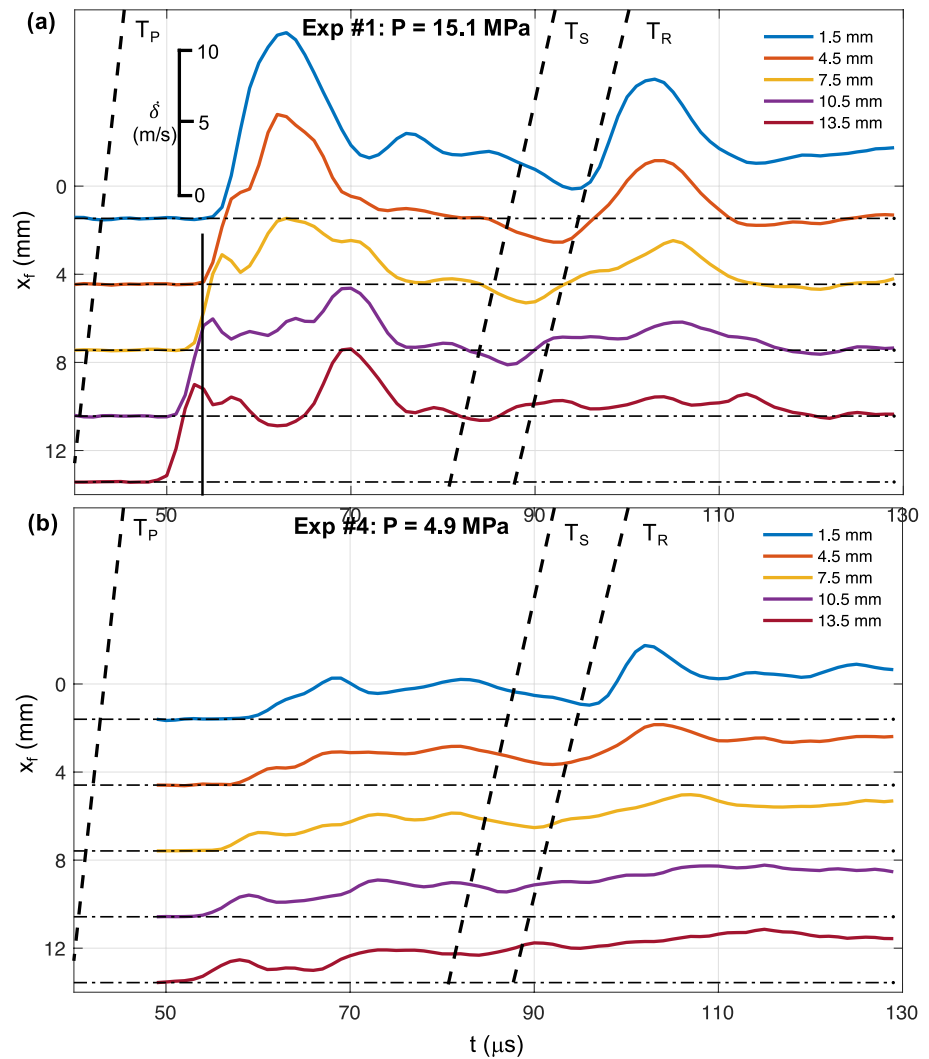
Figure 3. Slip rate versus time at five locations on the fault with different distances (x_f) from the free surface for (a) Exp #1 ($P = 15$ MPa) and (b) Exp #4 ($P = 4.9$ MPa). The locations are shown in Figure 2. Dashed lines marked with T_p, T_s, and T_R indicate the arrival times of P, S, and Rayleigh waves. Note that the peaks in $\dot{\delta}$ increase near the free surface for both the supershear rupture and the trailing Rayleigh. The lower level of applied loading P in Exp #4 results in a weaker rupture with smaller slip rates.

becomes asymmetric with respect to the fault, with peak values of 8 and 4.5 m/s at the hanging and foot walls, respectively. The walls slide in opposite directions, with small deviations from the orientation of the fault. After the rupture is reflected from the free surface ($t = 78$ μs), sliding continues at smaller particle velocities, with a sub-vertical motion of the hanging wall and motion at a dip of $\beta \approx 40°$ of the footwall. At this stage, the magnitude of accumulated surface displacements, $|\mathbf{u}_s|$, on the hanging wall ranges between $|\mathbf{u}_s| = 100$ μm near the fault and $|\mathbf{u}_s| = 90$ μm at $x_1 = 5$ mm, while that on the footwall ranges between $|\mathbf{u}_s| = 74$ μm near the fault and $|\mathbf{u}_s| = 65$ μm at $x_1 = -5$ mm (Figure 5).

Plots of particle velocity vectors along the surface at time intervals of 2 μs (Figure 6) show the rapid variations and significant rotations of $\dot{\mathbf{u}}_s$ during the interaction of the supershear rupture with the free surface in greater detail. As the supershear rupture arrives at the free surface ($t = 55$–59 μs), the surface velocity magnitude, $|\dot{\mathbf{u}}_s|$, initially increases at the right side of the hanging wall, then at smaller x_1. The rupture initially generates a velocity field that is rotated in a counter-clockwise fashion ($t = 55$–57 μs) relatively to the propagation direction. As it breaks the free surface ($t = 59$ μs), the hanging wall surface experiences clockwise rotation relatively to its previous state, while the footwall undergoes additional counter-clockwise rotation. At $t = 61$–63 μs, the hanging
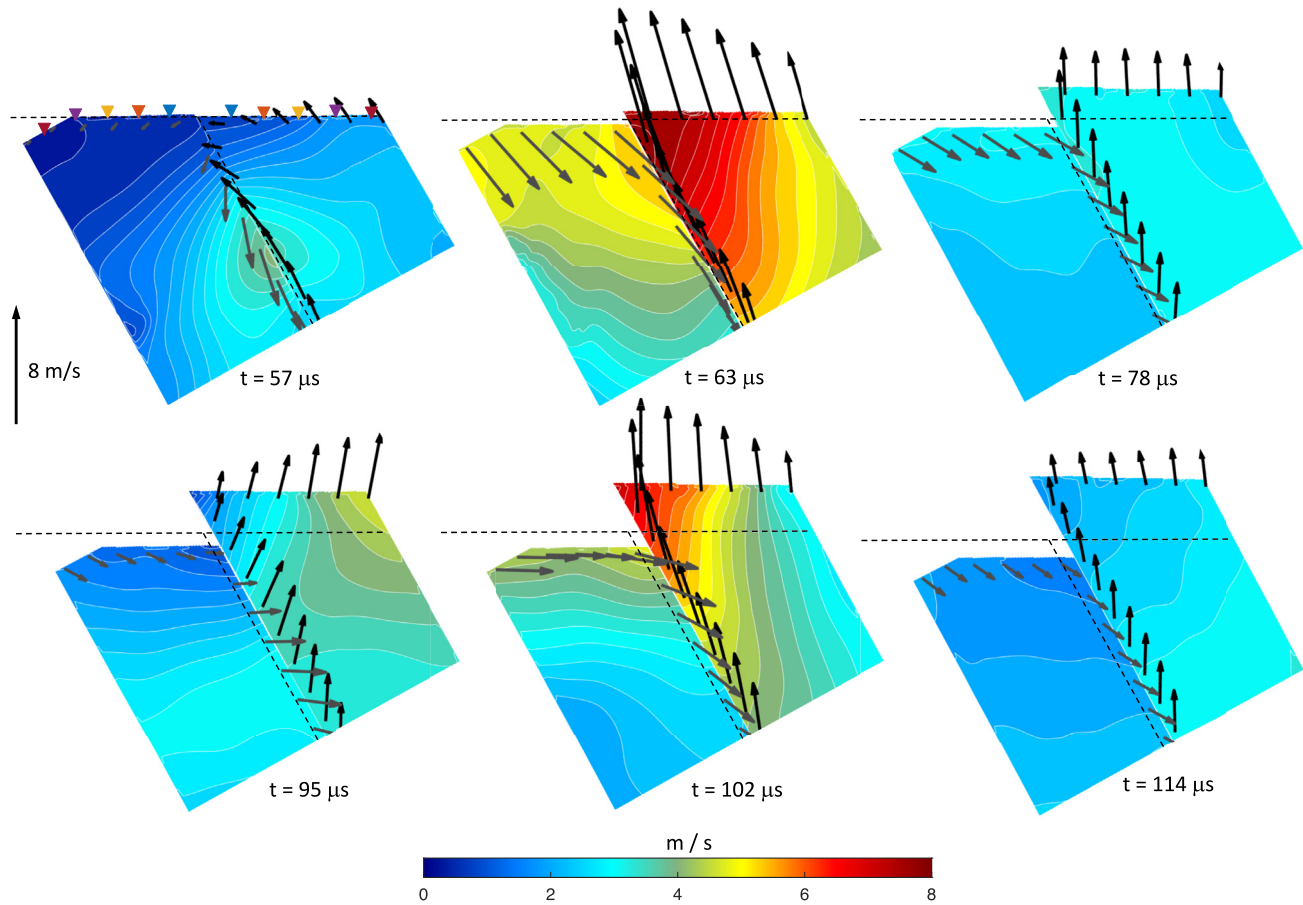
Figure 4. Snapshots of the particle velocity magnitude at different stages of Exp. #1 ($P = 15$ MPa), with overlaid vectors showing the direction and magnitude of particle velocities near the interface and at the free surface. The deformation is exaggerated by a factor of 10. The free surface generates asymmetry in the velocity field, with larger velocities at the hanging wall compared to the footwall. The first panel (top left) also shows the surface locations (color triangles) used in Figure 9 to study the attenuation of the ground motion with distance from the fault.

wall shows an additional increase in $|\dot{\mathbf{u}}_s|$, which starts near the fault and continues at locations with larger x_1. The rotations of $\dot{\mathbf{u}}_s$ continue in both walls, with a flapping of the hanging wall near the fault, in which the rotation near the fault is larger at $t = 61$ μs than at $t = 63$ μs. As the rupture is reflected from the free surface and propagates downward along the fault ($t = 65$–69 μs), $|\dot{\mathbf{u}}_s|$ generally decreases, with additional rotations into a nearly vertical motion of the hanging wall and right-downward of the footwall. A temporary additional rotation of $\dot{\mathbf{u}}_s$ with a decrease in $|\dot{\mathbf{u}}_s|$ is observed at $t = 71$–75 μs, especially at the footwall. As shown by plots of the average direction and magnitude of $\dot{\mathbf{u}}_s$ at different stages of the interaction of the supershear rupture with the free surface (Figure 7a), the foot wall shows a total counter-clockwise rotation of $\sim115°$ in the average direction of $\dot{\mathbf{u}}_s$ between $t = 57$ and 77 μs, while the hanging wall shows a clockwise rotation of $\sim80°$.

3.2.2. Trailing-Rayleigh Rupture

The trailing-Rayleigh rupture also generates increase in particle velocities with asymmetry between the hanging and footwalls, but the pattern and direction of the velocity field are different than those associated with the supershear rupture. The trailing-Rayleigh rupture approaches the free surface ($t = 95$ μs) with an elongated feature of increased fault-normal velocity at the bulk, which initially interacts with the free surface at the right part of the hanging wall, resulting in larger $|\dot{\mathbf{u}}|$ values at the upper-right corner rather than on the fault (Figure 4). At this stage, the velocity field near the fault is rotated such that the footwall moves horizontally and the hanging wall has both vertical and horizontal positive velocities. The interaction of the trailing-Rayleigh rupture with the free
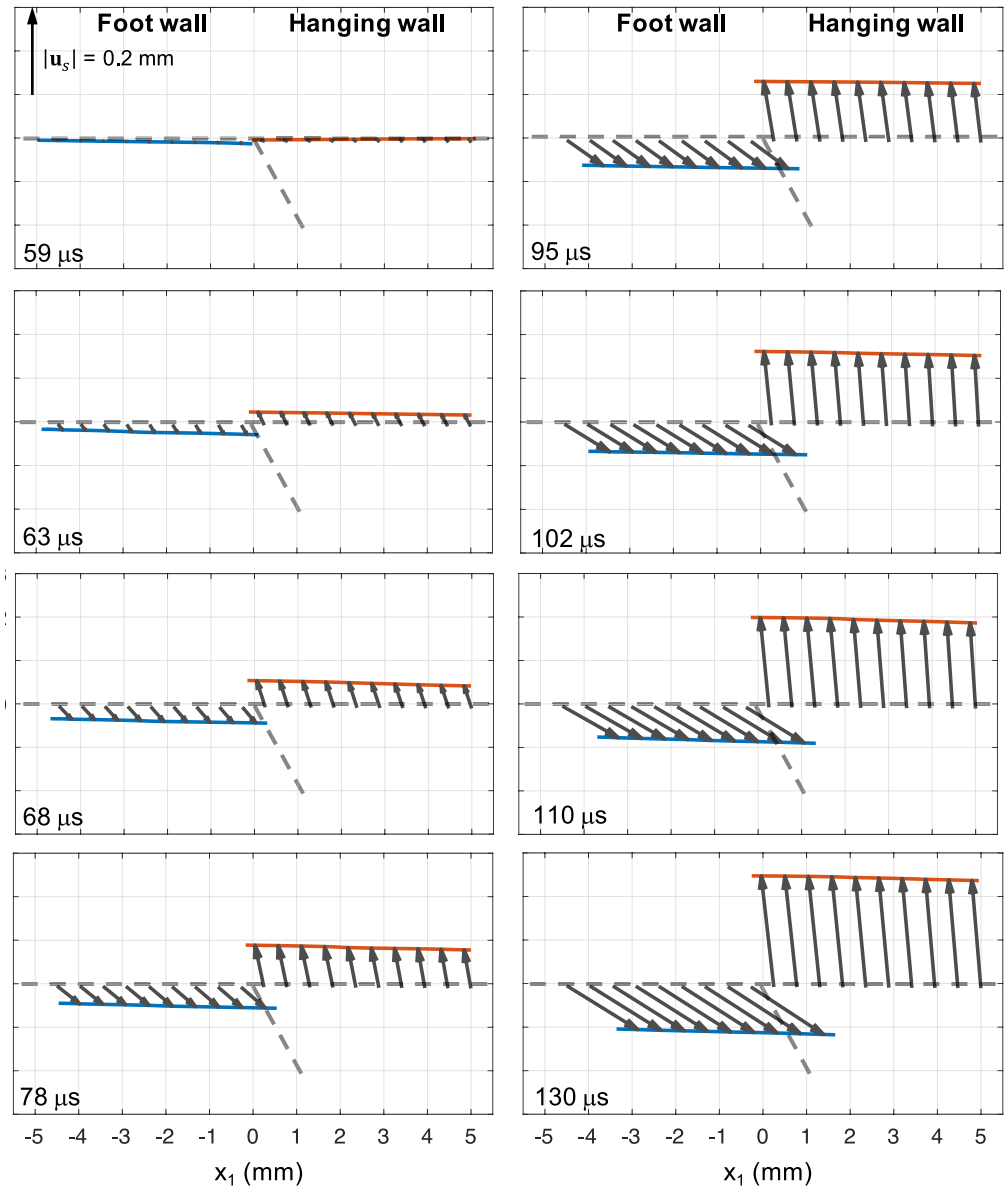
Figure 5. Snapshots of accumulated displacements along the surface, u_s, at different stages of Exp. #1 ($P = 15$ MPa). The vector sizes are amplified by a factor of 10. The left ($t = 59$–78 μs) and right ($t = 95$–130 μs) panels capture the interactions of the supershear and trailing Rayleigh ruptures with the free surface, respectively. The figure highlights the differences in $|u_s|$ between the hanging and footwalls, as well as the rotations of u_s throughout the experiment into motions that are nearly vertical at the hanging wall and at a dip of $\beta \approx 32°$ at the footwall.

surface ($t = 102$ μs) leads to an increase in $|\dot{u}|$, with larger values at the hanging wall (Figure 4). After reflection ($t = 114$ μs), sliding continues with smaller slip velocities. Because the camera records 128 images, we cannot measure the permanent surface deformation after a complete stop of the rupture, but observe the displacements up to $t = 130$ μs. At this stage, the values of $|u_s|$ on the hanging wall ranges between $|u_s| = 257$ μm near the fault and $|u_s| = 248$ μm at $x_1 = 5$ mm, while that on the footwall ranges between $|u_s| = 200$ μm near the fault and $|u_s| = 190$ μm at $x_1 = -5$ mm (Figure 5). Moreover, the directions of u_s are nearly vertical and at dip of $\beta \approx 32°$ for the hanging wall and footwalls, respectively.

The spatiotemporal evolution of $\dot{u}_s$ during the interaction of the trailing-Rayleigh rupture with the free surface is explored in greater detail in Figures 7b and 8. As it approaches the free surface ($t = 89$–93 μs), $\dot{u}_s$ decreases in magnitude and rotates counter-clockwise near the fault at both walls. At the arrival of the trailing-Rayleigh
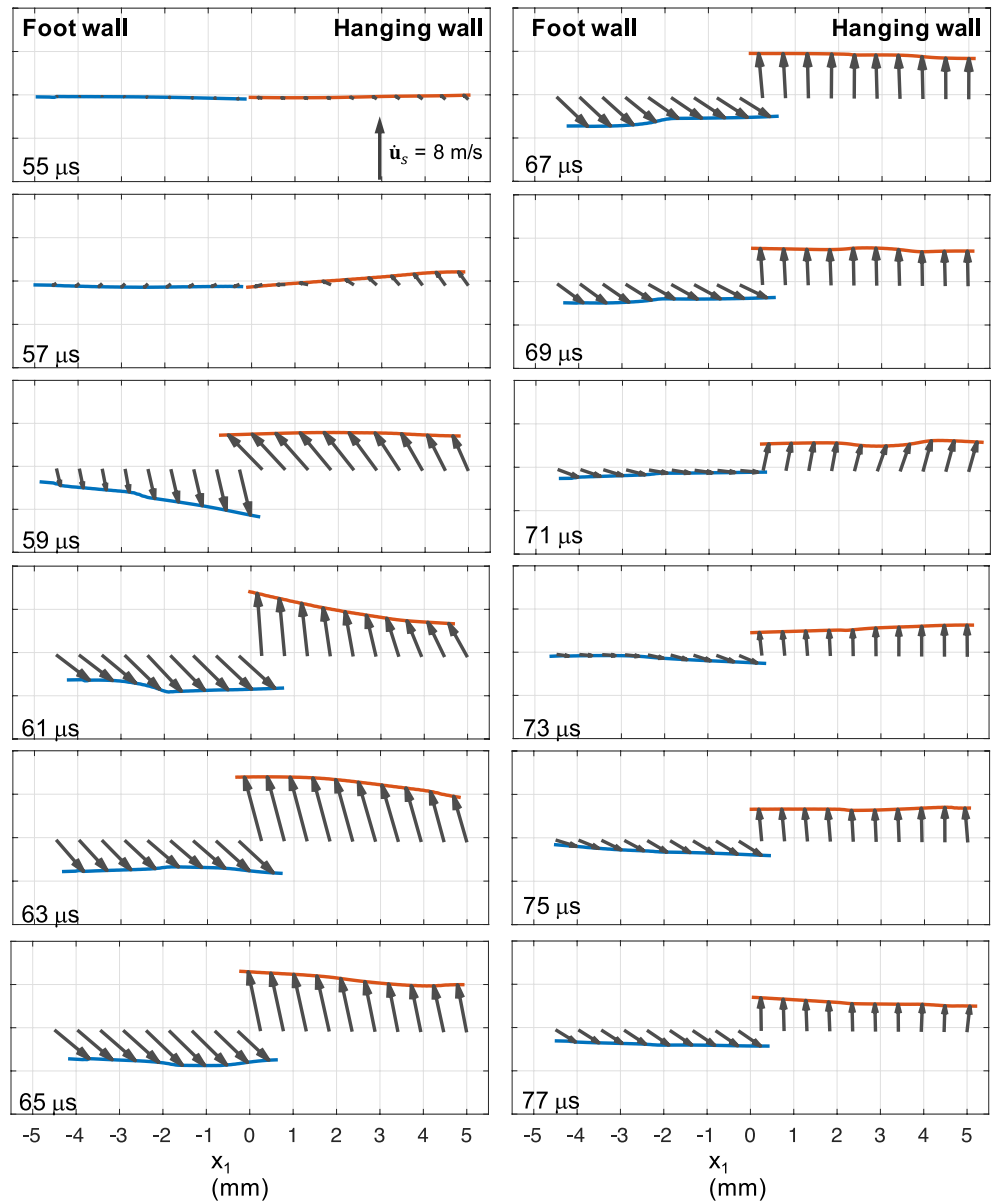
Figure 6. Snapshots of particle velocity vectors along the surface, $\dot{\mathbf{u}}_s$, during the interaction of the supershear rupture with the free surface in Exp #1 ($P = 15$ MPa). The interaction is associated with rapid temporal and spatial variations in $\dot{\mathbf{u}}_s$, as well as significant rotations.

rupture at the free surface ($t = 95$–97 μs), there is an increase in $|\dot{\mathbf{u}}_s|$ at the right side of the hanging wall, followed by a leftward propagation along the free surface, which is associated with counter-clockwise rotation of $\dot{\mathbf{u}}_s$ on the footwall into a sub-horizontal direction and clockwise rotation of the hanging wall. At $t = 99$–101 μs, $|\dot{\mathbf{u}}_s|$ increases along the footwall and at the hanging wall near the fault, with larger values at the latter. Between $t = 103$ and 111 μs, $|\dot{\mathbf{u}}_s|$ decreases and the direction of $\dot{\mathbf{u}}_s$ generally changes back to the one prior to the arrival of the trailing Rayleigh.

3.2.3. Attenuation With Distance From the Fault in the Near Field

To examine how the ground motions vary with distance from the fault, Figures 9 and 10 show the vertical ($\dot{\mathbf{u}}_2$) and horizontal ($\dot{\mathbf{u}}_1$) velocity traces at different locations on the surface, respectively. The traces reflect the changes in magnitude and direction of the surface velocities during the interactions of the supershear rupture and the
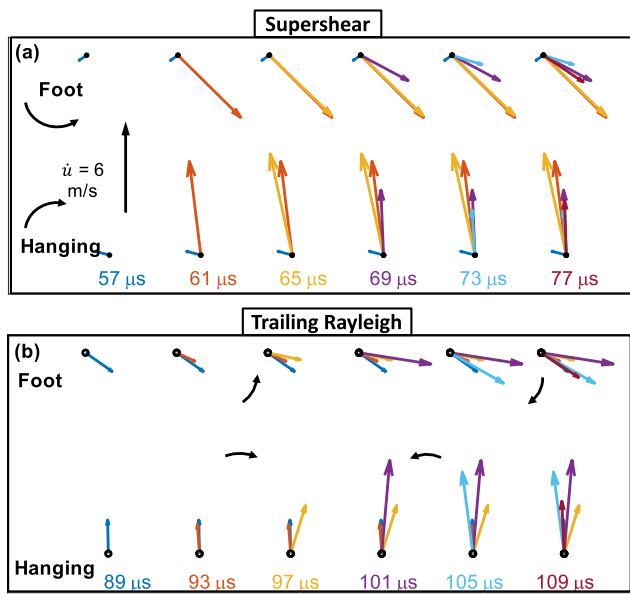
Figure 7. Temporal variations of the direction and magnitude of average surface velocities at the hanging and footwalls during the interaction of the supershear rupture (a) and trailing Rayleigh (b) with the free surface. In order to avoid masking dominant local behavior, each vector represents the average surface velocities of the points between $x_1 = 0$ and 2 mm for hanging wall (lower row in each subplot) and between $x_1 = -2$ and 0 mm for the footwall (upper row in each subplot). The interaction of the supershear rupture with the free surface is associated with clockwise and counter-clockwise rotations at the hanging and footwalls, respectively. The trailing Rayleigh generates additional, temporal, rotations at the same directions.

trailing-Rayleigh rupture with the free surface (Figures 6–8) and vary significantly between the hanging and footwalls, between the supershear and the trailing-Rayleigh rupture, and at different distances from the free surface.

The traces of $\dot{u}_2$ are asymmetric with respect to the fault, with larger peaks at the hanging wall. As the distance from the fault increases, there are changes in the structure of the traces, which are generally associated with a decrease in the peaks of $\dot{u}_2$. The surface motions generated by the supershear rupture begin at $x_1 = 5$ mm, then continue along the rest of the free surface over 4 μs, as indicated by the black dashed arrow labeled T_{Rup}. Note that, because of the rotated velocity field ahead of the rupture tip (Figure 4), the onset of the motions is better observed at the $\dot{u}_1$ traces in Figure 10. At the traces along the hanging wall, $\dot{u}_2$ initially increases to a value ~4 m/s ($t = 59$ μs), with a more rapid acceleration near the fault (Figure 9), then there is an additional increase in $\dot{u}_2$ to a peak value at $t = 63$ μs near the fault and later at larger x_1. The peaks decrease with x_1, from a value of $\dot{u}_2 = 7.4$ m/s at $x_1 = 1$ mm to a value of $\dot{u}_2 = 5.9$ m/s at $x_1 = 5$ mm (Figures 11a). At the footwall, the shape of the traces gradually changes with distance from the fault (Figure 9) and the peaks in $\dot{u}_2$ decrease from a value of $\dot{u}_2 = -5$ m/s at $x_1 = -1$ mm ($t = 60$ μs) to a value of $\dot{u}_2 = -3.6$ m/s at $x_1 = -5$ mm ($t = 63$ μs). Because of the change in shape of the traces, the value of the negative peaks does not decrease continuously as x_1 decreases (Figures 11a).

As indicated by the black dashed arrow labeled T_{TR} in Figure 9, the surface motions generated by the trailing-Rayleigh rupture also begin at $x_1 = 5$ mm and continue along the rest of the free surface over 4 μs. The peaks in $\dot{u}_2$ during the interaction of the trailing-Rayleigh rupture with the free surface are smaller than during that of the supershear rupture. The traces at the hanging wall vary with x_1, with a transition from a single peak of $\dot{u}_2 = 6.6$ m/s at $x_1 = 1$ mm ($t = 102$ μs), into two separated peaks of $\dot{u}_2 = 4.6$ m/s at $x_1 = 5$ mm. The traces at the footwall barely vary with x_1 and show smaller (negative) peaks, ranging between 2.1 and 2.3 m/s (Figures 11a).

A noteworthy observation is that the traces of $\dot{u}_1$ show larger values at the footwall for both the supershear and trailing Rayleigh ruptures (Figures 10 and 11b). This is consistent with the, overall, nearly vertical motion of the hanging wall and right-downward motion of footwall shown in Figures 6–8. During the interaction of the supershear rupture with the free surface, the magnitude of the negative peaks of $\dot{u}_1$ at the hanging wall decrease from a value of $|\dot{u}_1| = 3.8$ m/s at $x_1 = 1$ mm to a value of $|\dot{u}_1| = 2.4$ m/s at $x_1 = 5$ mm, while the traces of the footwall show small variation with x_1, with positive peaks that range between $\dot{u}_1 = 4$ and 4.2 m/s. Moreover, the peaks of the traces at $x_1 = 1$ and 2 mm at the hanging wall are significantly narrower than those at the footwall. During the interaction of the trailing-Rayleigh rupture with the free surface, the hanging wall shows a transition to positive values of $\dot{u}_1$ with peaks that range between $\dot{u}_1 = 1.4$ and 1.1 m/s. At the footwall, the peaks are slightly larger during the interaction of the trailing Rayleigh than during that of the supershear, with peaks that ranges between $\dot{u}_1 = 4.7$ and 4.4 m/s.

3.3. Effect of the Static Pre-Stress on Ground Motion

To test the effect of compressive load on ground motion, we conducted three additional experiments under lower far field stresses of $P = 10$, 7.4 and 4.9 MPa. These stress levels result in larger sub-Rayleigh to supershear rupture transition distances and serve to examine various scenarios of the interaction of the transitioned ruptures with the free surface. The temporal evolution of $\dot{u}_1$ and $\dot{u}_2$ in those experiments is qualitatively consistent with that in Exp. #1, but, as P decreases, the ruptures transition to supershear speeds occurs closer to the free surface, resulting in weaker supershear fronts that generate smaller surface velocities (Figure 12).
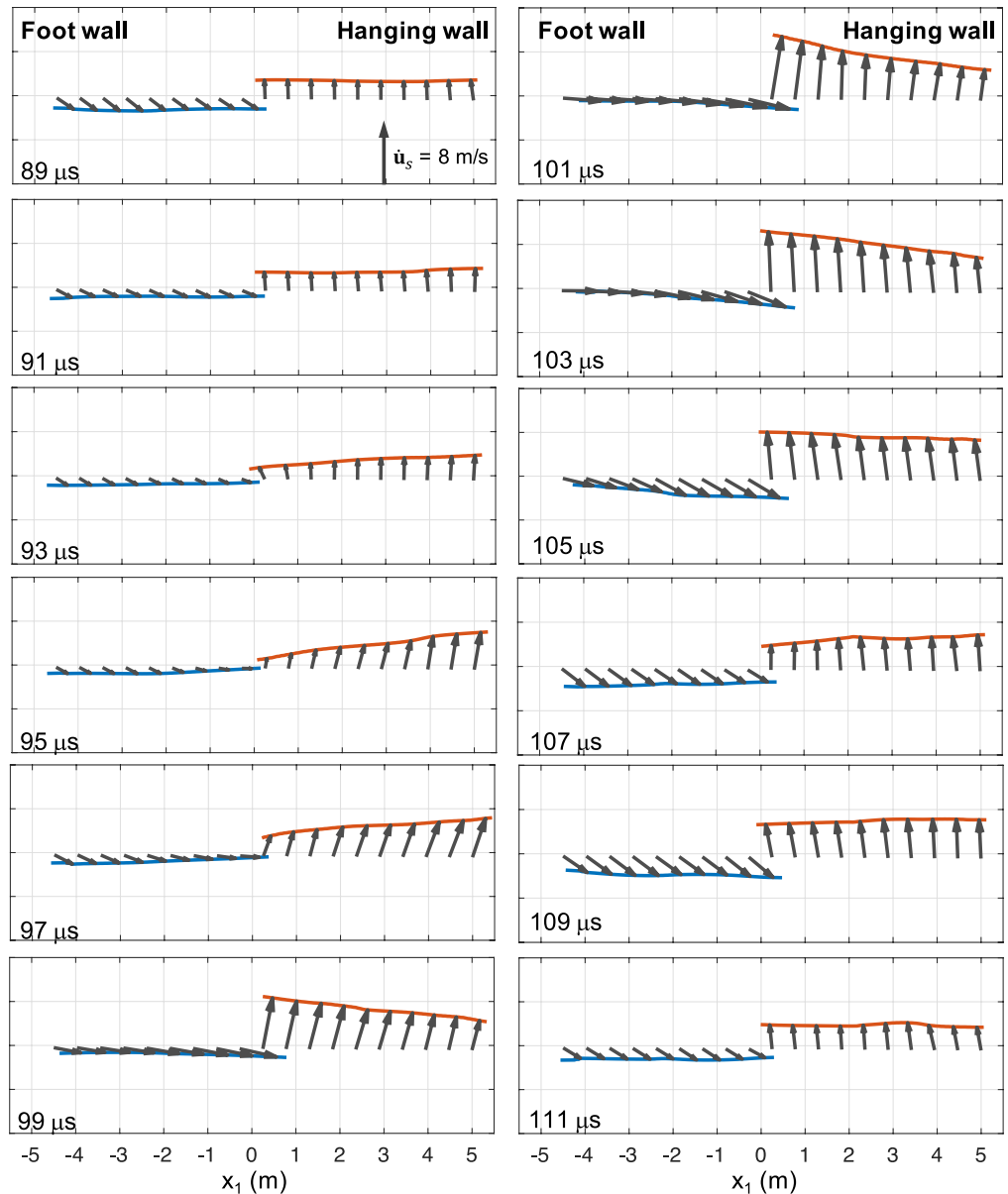
Figure 8. Snapshots of velocities vectors along the surface during the interaction of the trailing Rayleigh with the free surface in Exp #1 ($P = 15$ MPa). The interaction leads to temporal magnitude increase and rotations in $\dot{\mathbf{u}}_s$. Note the sub-horizontal motion of the footwall at $t = 99$–101 μs.

For experiments under $P \leq 7.4$ MPa, the trailing-Rayleigh rupture is more dominant than the supershear rupture itself, with larger peaks in both $\dot{u}_1$ and $\dot{u}_2$. In Exp. #4, which was performed under the lowest load of $P = 4.9$ MPa, the supershear rupture generates a peak vertical velocity of $\dot{u}_2 = 2$ m/s at $x_1 = 1$ mm, while the trailing-Rayleigh rupture generates a peak of $\dot{u}_2 = 4.5$ m/s. Discrete velocimeter measurements from previous rupture experiments (Gabuchian et al., 2014, Figure 9) show that, under similar load but smaller distance of the nucleation location from the free surface ($x_f = 7.4$ cm) and weaker nucleation intensity (discharge of 1.5 kV, instead of 2 kV used here), the rupture arrives at the free surface at a sub-Rayleigh speed, without evolving into a supershear rupture. Gabuchian et al. (2014) also performed several experiments under larger load of $P = 15$ MPa. Despite the smaller distance to the nucleation point, weaker nucleation process, and different measurement technique, the temporal evolution of $\dot{u}_2$ in these experiments is similar to that in Exp. #1 of this study (Figure 12), indicating that once ruptures are well-developed their propagation is controlled by the level of applied static pre-stress.
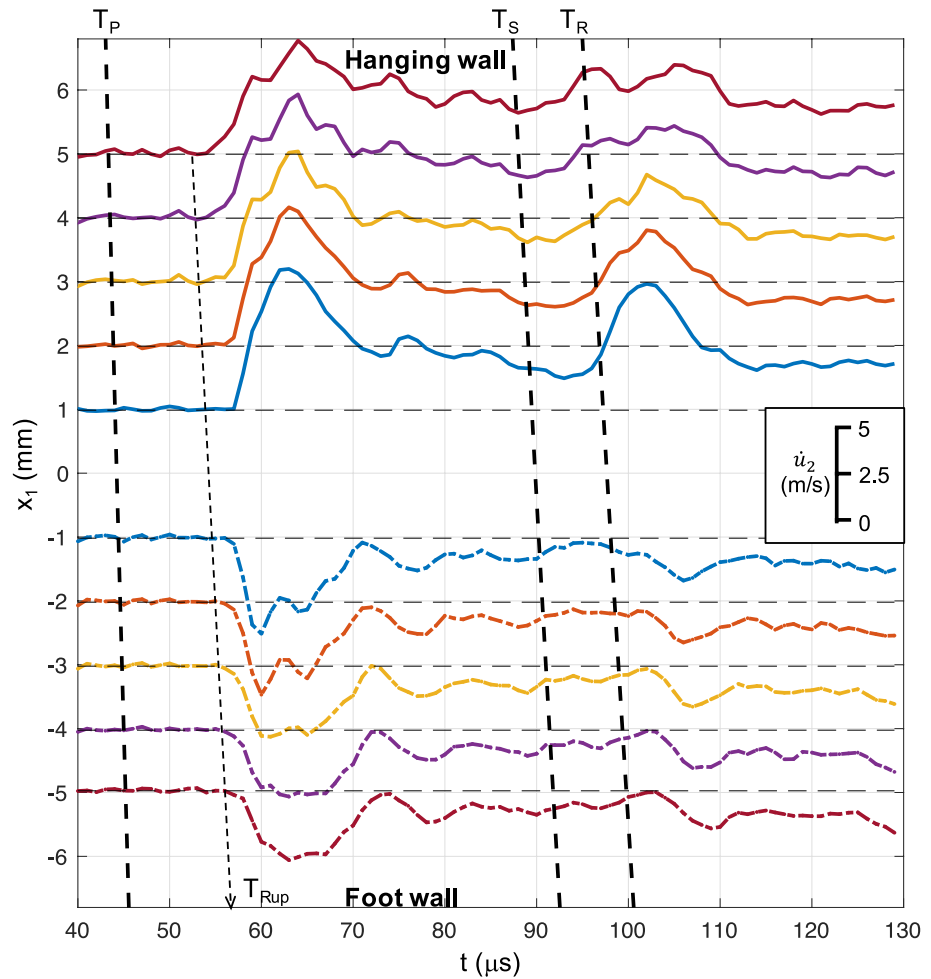
Figure 9. Traces of vertical velocities ($\dot{u}_2$) at 10 locations along the surface for Exp #1 ($P = 15$ MPa). The locations are shown in Figure 4. Dashed lines marked with T_p, T_s, and T_R indicate the arrival times of P, S, and Rayleigh waves. The black dashed arrow labeled T_{Rup} corresponds to the time when the rupture starts to generate surface motion at a given location. The traces are asymmetric with respect to the fault, and change structure with distance from the fault.

The absolute maximum velocities $\dot{u}_{2,\text{max}}$ and $\dot{u}_{1,\text{max}}$ at each location along the surface during the interactions of the supershear and trailing Rayleigh ruptures with the free surface are summarized in Figure 13 for the four experiments considered in this study. The values of $\dot{u}_{2,\text{max}}$ and $\dot{u}_{1,\text{max}}$ generally decrease with P, but variations of $\dot{u}_{2,\text{max}}$ and $\dot{u}_{1,\text{max}}$ with x_1 are generally similar between different experiments, including the hanging wall versus footwall effects. All experiments show larger $\dot{u}_{2,\text{max}}$ values at the hanging wall than at the footwall. The values of $\dot{u}_{1,\text{max}}$ are generally larger at the footwall, with the exception of supershear fronts of Exp. #3 and #4 for which $\dot{u}_{1,\text{max}}$ is similar for the hanging wall and the footwall. Note that, in those experiments, the supershear rupture is less intense than the trailing Rayleigh rupture. In general, $\dot{u}_{2,\text{max}}$ show larger attenuation with $|x_1|$ than $\dot{u}_{1,\text{max}}$, and there are more significant attenuations at hanging wall than at the foot wall. In all experiments, $\dot{u}_{2,\text{max}}$ decays with x_1 at hanging wall. At the footwall, it decays with $|x_1|$ only during the supershear ruptures of Exp. #1 and 2, but does not vary with x_1 in other cases. $\dot{u}_{1,\text{max}}$ generally decays with x_1 at the hanging-wall during supershear and at the foot wall during the trailing Rayleigh, but does not vary with distance in other cases.

4. Discussion

4.1. Upscaling and Implications for Natural Faults

The first systematic study of scaling of near-fault laboratory measurements of ground velocities to those from a specific well-documented earthquake was performed by Mello et al. (2014) who were able to reproduce in the
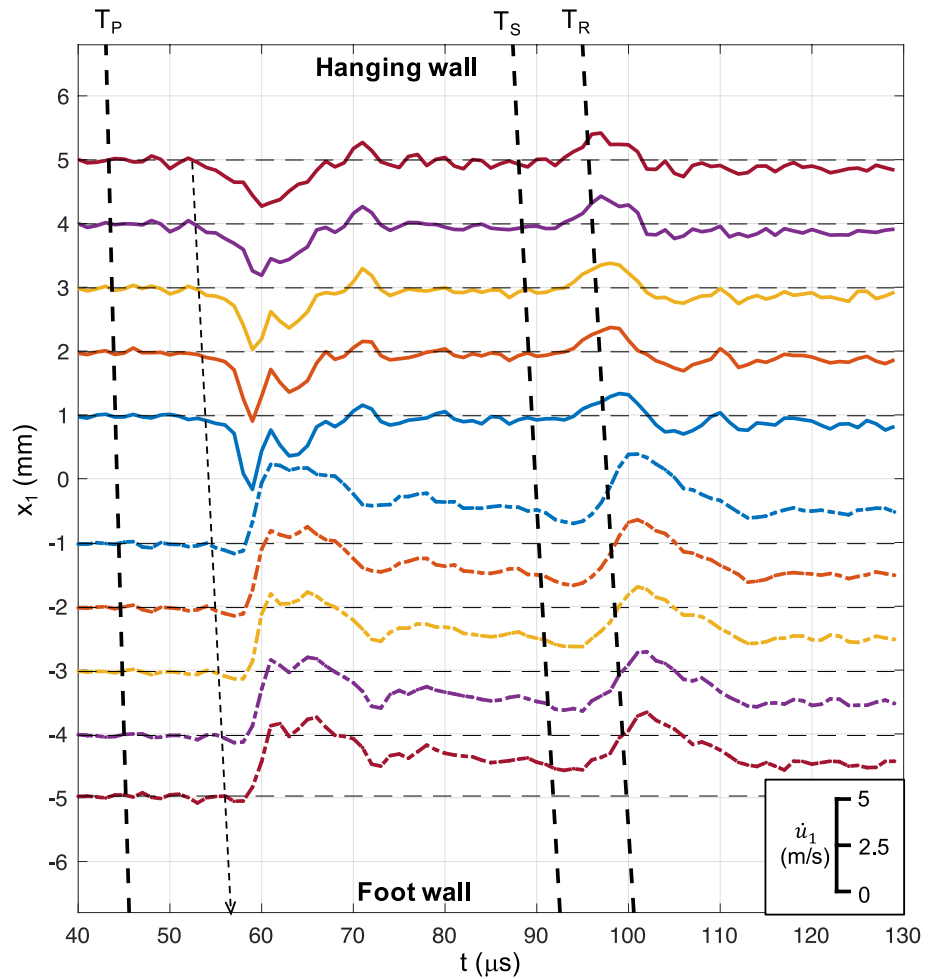
Figure 10. Traces of horizontal velocities ($\dot{u}_1$) at 10 locations along the surface during Exp #1 ($P = 15$ MPa). The locations are shown in Figure 4. Dashed lines marked with T_p, T_s, and T_R indicate the arrival times of P, S, and Rayleigh waves. The black dashed arrow labeled T_{Rup} corresponds to the time when the rupture starts to generate surface motion at a given location. The traces are asymmetric with respect to the fault. The traces of $\dot{u}_1$ show less variability with distance from the fault than those of $\dot{u}_2$.
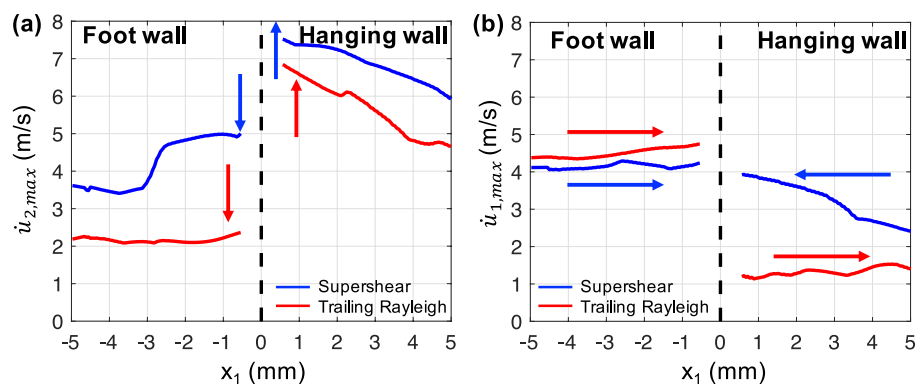

Figure 11. Absolute maximum of $\dot{u}_2$ (a) and $\dot{u}_1$ (b) as a function of the location along the surface during the supershear rupture (blue) and trailing Rayleigh (red) of Exp #1 ($P = 15$ MPa). The arrows show the corresponding motion directions of the hanging and footwall. The hanging wall shows larger values of $\dot{u}_2$, while the footwall shows larger values of $\dot{u}_1$. There is generally larger attenuation with $|x_1|$ at the hanging wall than at the footwall and for $\dot{u}_2$ than for $\dot{u}_1$.
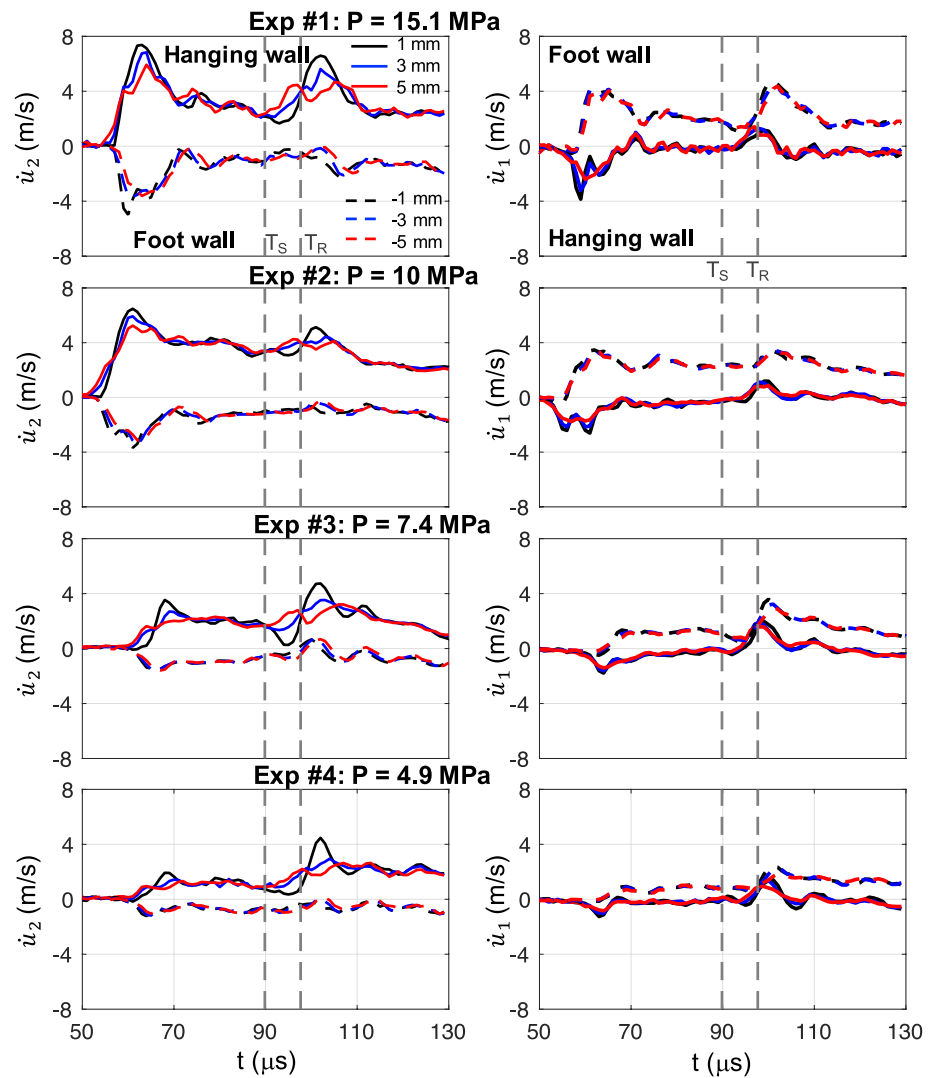
Figure 12. Vertical (left) and horizontal (right) surface velocities versus time at six locations on the surface for the four experiments reported in this study. Dashed lines marked with T_s and T_R indicate the arrival times S and Rayleigh waves to the surface at $x_1 = 0$. The qualitative behavior in Exp. #2–4 is consistent with that in Exp. #1. However, as P decreases, the ruptures arrive later at the free surface and generate smaller surface velocities, with a a transition from a dominant supershear rupture to a dominant trailing-Rayleigh rupture.

laboratory the full time histories of each of the three velocity components recorded at the Pump Station-10 during the strike-slip, supershear 2002 Denali earthquake. This comparison was enabled by utilizing the theoretical observation (Rosakis et al., 2020; Samudrala et al., 2002) that near-field particle velocity fields of any steady state rupture scale as $c_s\Delta\sigma_0/\mu$, where $\Delta\sigma_0$ is the dynamic shear stress drop, in all available analytical cohesive zone rupture models of fast frictional rupture irrespective of rupture speed regime and frictional law (e.g., Rice et al., 2005; Samudrala et al., 2002). They also scaled time by shear wave speeds and by requiring that supershear transition lengths remain similar.

For the thrust configuration presented here, let us discuss scaling of the maximum amplitudes of our experimentally obtained displacement and velocity histories by using a slightly different scaling methodology that, in addition to comparing with the few available near field measurements, allows us to compare our experimental results to available numerical models of thrust fault events. It is important to note that the choice of how to normalize the measured quantities is non-unique and it may depend on the particular problem at hand. A useful insight comes from considering ruptures that have effective linear slip-weakening behavior, as measured for our interfaces (Rubino et al., 2017) and often assumed in modeling earthquake ruptures (Ide & Takeo, 1997;
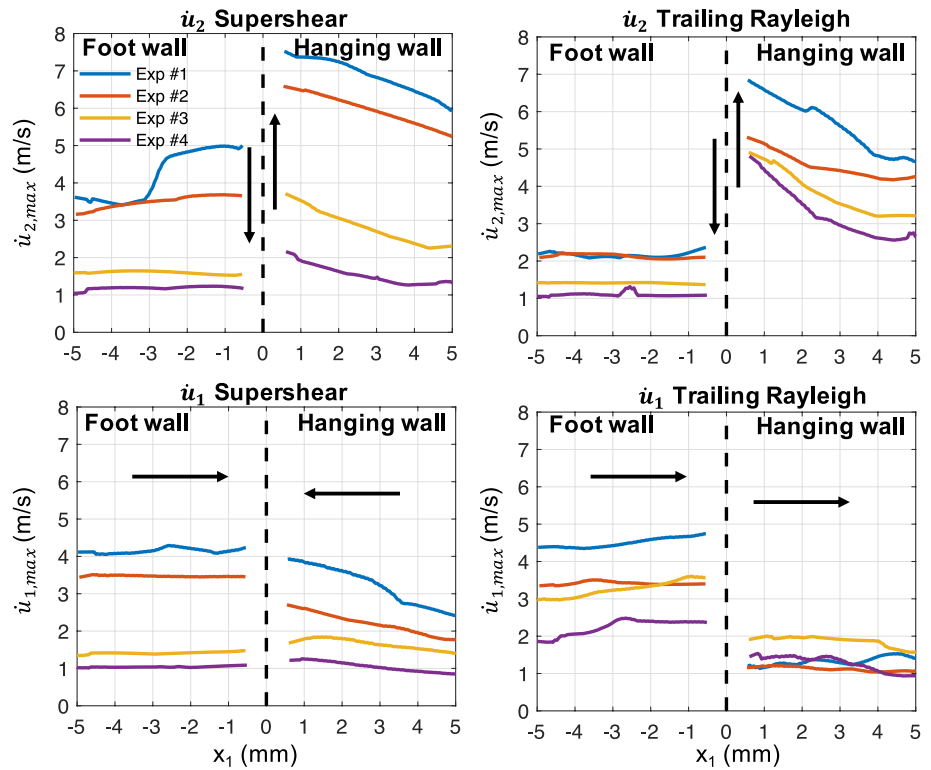
Figure 13. Absolute maximum of $\dot{u}_2$ (top row) and $\dot{u}_1$ (bottom row) during the supershear rupture (left) and trailing Rayleigh (right) for the four experiments performed in this study with load levels of $P = 15.1$ (Exp. #1), 10 (Exp. #2), 7.4 (Exp. #3), and 4.9 (Exp. #4) MPa. Note that surfaces velocities are governed by the pre-stress level. In addition to smaller stress drops for smaller loads and hence smaller shear and normal stresses on the fault, the sub-Rayleigh to supershear transition distance generally increases as P decreases, and the rupture speed after the transition generally decreases as P decreases.

Kanamori & Brodsky, 2004; Ma & Beroza, 2008; Oglesby et al., 1998, 2000). Here, we consider the dimensionless form defined in Scala et al. (2019), in which the dimensionless distance is defined as $\tilde{x} = \frac{\Delta\sigma_0}{\mu D_c}x$, where D_c is the effective slip weakening distance over which shear stress decreases from its peak to dynamic value; the dimensionless displacement as $\tilde{u} = u/D_c$; the dimensionless time as $\tilde{t} = \frac{c_s \Delta\sigma_0}{\mu D_c}t$, where $\Delta\sigma_0$ is the dynamic stress drop; and the dimensionless velocity as $\tilde{v} = \frac{\mu}{c_s \Delta\sigma_0}\dot{u}$. The expression for the dimensionless velocity has been used by Rosakis (2002) for the scaling of experiments and by Dunham and Bhat (2008) to scale the results of fully 3-D computations of ruptures in a thrust fault configuration. However, the other dimensionless expressions for time and length are different because the above-mentioned studies used the vertical fault width in a strike slip configuration as a normalizing length scale, which is not well-defined in our two dimensional, thrust fault experimental setup. Note that the term $\frac{\mu D_c}{\Delta\sigma_0}$ is proportional to the cohesive zone size at the rupture tip, R_0, estimated by Palmer and Rice (1973) for linear slip-weakening friction. Based on a plot of shear stress versus time for the same experiment (Tal et al., 2020), we estimate a dynamic stress drop value of $\Delta\sigma_0 = 3$ MPa for Exp. #1, which is consistent with seismological estimates of static stress drops. Although the experiment was fitted with a formulation of rate-and-state friction with enhanced weakening in Tal et al. (2020), the effective friction showed an initial weakening over a sliding distance of 25 μm, thus we estimate an effective slip weakening distance of $D_c \sim 25$ μm. The dynamic shear wave speed and shear modulus of Homalite are $c_s = 1.28$ km/s and $\mu = 1.96$ GPa, respectively (see Section 2).

The dimensionless experimental quantities are consistent with numerical simulations and observational data. Substituting peak particle velocity magnitudes of $|\dot{u}_{max}| = 8.6$ and 6.5 m/s for the hanging and footwalls during Exp. #1, gives dimensionless peak velocities of $\tilde{v} \sim 4.4$ and 3.3, respectively. We now use these dimensionless estimates to compute upscaled velocity levels and compare them with the numerical simulations of Ma and Beroza (2008), considering only the simulations of thrust faults in homogenous medium. For the values of $c_s = 3.464$ km/s, $\Delta\sigma_0 = 2.4$ MPa, and $\mu = 32$ GPa used in the simulations of Ma and Beroza (2008) for a thrust

fault in a homogenous medium, the dimensionless experimental quantities above are equivalent to peak velocities of 1.14 and 0.86 m/s. These values are consistent with simulation results of Ma and Beroza (2008) for a thrust fault with dip angle of 60° in a homogenous medium, which show peak particle velocities of 1.8 and 1.18 m/s at the hanging and footwalls, respectively. The peak velocity magnitudes would increase at the hanging and foot-walls for smaller dip angles (Ma & Beroza, 2008; Oglesby et al., 1998, 2000). Peak surface velocities on the same order of magnitude were also observed at near fault stations during the 1999 Chi-Chi (e.g., Shin & Teng, 2001) and 2008 Wenchuan earthquakes (e.g., Liu & Li, 2009).

The width of the high-velocity feature during the interaction of the supershear and the trailing Rayleigh ruptures is $t \sim 13$ μs (Figures 9 and 10), which is equivalent to a dimensionless time of $\tilde{t} \approx 1$ with the experimental values of $D_c = 25$μm, $\Delta\sigma_0 = 3$MPa, $c_s = 1.28$ km/s, and μ = 1.96 GPa. Up-scaling of the time requires determination of the equivalent slip weakening distance for large earthquakes, which is not well constrained (Kanamori & Brodsky, 2004). For the frictional and bulk properties used in the simulations of Ma and Beroza (2008) ($D_c = 0.15$ m), a dimensionless time of $\tilde{t} \approx 1$ yields a velocity peak width of ~0.5 s, which is consistent with the actual widths observed in the simulations. In our experiments, we observed the surface velocities up to a distance of ~5 mm from the fault, which yields a dimensionless distance of $\tilde{x} = 0.3$ and x ~ 0.5 km for the parameters used by Ma and Beroza (2008) when simulating homogenous medium. For the 1995 Kobe earthquake, Ide and Takeo (1997) estimated a weakening distance of 0.5 m, which for $\tilde{x} = 0.3$, yields a distance to 1.5 km from the fault. Nevertheless, this analysis shows that, with the FOV of our experiments, we observe the motion close to the fault. A larger FOV would allow us to observe the velocities at larger distances, but at the cost of lower resolution and less accurate dynamic full-field measurements near the fault.

Similarly to field observations and numerical models (e.g., Abrahamson & Somerville, 1996; Allen et al., 1998; Chang et al., 2004; Nason, 1973; Shin & Teng, 2001; Steinbrugge et al., 1975) and numerical models (e.g., Duan & Oglesby, 2005; Ma & Beroza, 2008; Oglesby & Day, 2001; Oglesby et al., 1998, 2000; Scala et al., 2019; Shi et al., 1998), the experimentally observed surface motions during the interaction of the supershear rupture and the trailing Rayleigh with the free surface show substantial asymmetry between the hanging wall and footwall, with the hanging wall experiencing larger velocity magnitudes. However, as a result of the nearly vertical motion of the hanging-wall and right-downward motion of the foot wall (with temporal sub-horizontal motion during for the trailing Rayleigh; Figures 6–8), the footwall generally show larger horizontal velocity than the hanging wall (Figure 13) for the dip angle of $\beta = 61°$ considered in our experiments. This is consistent with simulations of Duan and Oglesby (2005) for trust faults with a dip angle of 45°, which showed dominant vertical component of ground motion at the hanging wall, but dominant horizontal component at the footwall. It is also consistent with the seismological observations from the 2008 Wenchuan earthquake (Zhang et al., 2019), in which the hanging wall effect was more evident in the vertical component than the horizontal component. The observation of larger horizontal velocities at the footwall has important implications for seismic risk in proximity to thrust faults, as buildings and infrastructure can have different sensitivity to the horizontal component of surface velocities than the vertical component.

Finally, a word of caution is in order regarding the direct comparison of the scaled experimental results to the above-mentioned numerical models and field observations. Strictly speaking, most of the above-mentioned studies did not feature supershear ruptures reaching the free surface. As a result, the comparison with the existing numerical studies as well as those with sparse field measurements, which may or may not have featured super-shear ruptures, have to be interpreted as only "qualitative" and only providing an "order of magnitude", albeit interesting, comparisons. In addition, the static pre-stresses in the experiments are depth-independent, while in the field, the stresses vary with depth due to gravitational body forces. Depth-varying pre-stresses may affect the ruptures as they propagate upward along the fault. However, in the near-surface region analyzed in this study, we expect that the geometrical effect of the wave interaction with the free surface on the rupture behavior and ground motion would be more significant than the effect of a depth varying pre-stress field.

4.2. Torqueing Mechanism of Thrust Faults

Based on a combination of laser velocimetry measurements and numerical simulations of thrust fault ruptures, Gabuchian et al. (2017) observed that a torqueing mechanism leads to reduction in normal stress and large slip near the free surface as theorized by Madariaga (2003). The simulations in Gabuchian et al. (2017) showed that a torque is generated by pronounced rotation of the hanging-wall wedge as the rupture initially approaches the

free surface. As the rupture breaks the free surface, the torque is released, resulting in the unclamping and the hanging-wall wedge. However, the measurements performed in Gabuchian et al. (2017) did not have the capacity to also investigate this phenomenon experimentally. In contrast, the use of DIC in the present study allows us to resolve this issue experimentally. Indeed, the vector plots of surface velocities in Figures 4, 6–8 enable us to observe and quantify the rotations during the interactions of the supershear and trailing Rayleigh ruptures with the free surface and demonstrate the existence of the mechanism with direct experimental measurements.

As the rupture in Exp. #1 approaches the free surface ($t = 55$–57 μs), it generates a torque via a counter-clockwise rotation of the velocity field ahead of the rupture tip (Figures 4, 6 and 7a). The torque is then released during the interaction of the rupture with the free surface ($t = 59$–70 μs), as the hanging wall surface experiences clockwise rotation into a sub-vertical motion, while the footwall undergoes additional counter-clockwise rotation into a motion at a dip of $\sim 30°$. As shown by the larger rotation near the fault at $t = 61$ μs than at $t = 63$ μs and the increase in the amplitude of surface velocities, the dynamic release of the torque is associated with a flapping of the hanging wall near the fault. Such motion is generally consistent with that observed in the foam rubber experiments of Brune (1996), although the flapping response here is significantly smaller because of the differences in experimental configuration and material properties, and there is no complete detachment of the hanging wall. Measurements of the fault-normal stress during the same Exp. #1 (Tal et al., 2020, Figure 3b) show that this process is associated with normal stress reduction from 13.5 to 8 MPa near the free surface.

Because the hanging and footwalls already slide at the time of the arrival of the trailing- Rayleigh rupture to the free surface, it is harder to examine the torqueing mechanism during its interaction with the free surface. The vector plots in (Figures 7b and 8) do show the generation of a torque via small counter-clockwise rotations of the hanging wall near the fault at $t = 93$ μs and its release via clockwise rotations of the hanging wall during the next ~ 8 μs. This process is associated with an additional, temporal, reduction in normal stress to a minimum value of 5 MPa at $t = 100$ μs (Tal et al., 2020, Figure 3b). Note that in Exp. #3 and #4, which are performed under smaller compressive load of P ≤ 7.4 MPa, the interaction of the trailing-Rayleigh rupture with the free surface leads to a temporary complete release of the normal stress.

5. Conclusions

Using an experimental technique that couples ultrahigh-speed photography with the DIC method, we have characterized the dynamics of transitioned supershear laboratory thrust earthquakes near the surface and the resulting near-field ground motion. The technique provides full-field quantities of particles velocities and displacements at time intervals of 1 μs during the interaction of updip supershear ruptures and subsequent trailing-Rayleigh rupture with the free surface and enables us to directly relate the near-field ground motion to the state of the rupture on the fault. Experiments under different initial loads show similar qualitative behavior. However, as the load decreases, the ruptures become weaker, transition to supershear speeds at a smaller down-dip distance, and generate smaller surface velocities. Moreover, for loads of $P \geq 10$ MPa, the supershear rupture front generates larger surface velocities than the trailing-Rayleigh rupture, while for loads of $P \leq 7.4$ MPa, the trailing-Rayleigh rupture generates larger surface velocities. Nondimensional analysis shows that the experimental results are in the order-of-magnitude agreement with larger-scale numerical simulations, as well as with near-field observations from thrust earthquakes, and thus can be used to enhance our understanding of the near-field ground motion, dynamics of natural thrust earthquakes, and seismic hazard.

Consistent with field observations and numerical models, the experimental surface motions show asymmetry between the hanging and footwalls during the interaction of both the supershear and the trailing Rayleigh ruptures with the free surface, with larger velocity magnitudes at the hanging wall. However, for the dip angle of $\beta = 61°$ considered in our experiments, the motion of the hanging wall is generally a nearly vertical motion, while that of the footwall is at a dip direction which is shallower than the dip angle of the fault. That leads to larger horizontal surface velocities at the footwall than at the hanging wall. The attenuation in surface velocity with distance from the fault is generally larger at hanging wall than at the footwall and for the vertical component than for the horizontal one.

Measurements of the rotations in surface motions during the interaction of the ruptures with the free surface confirm experimentally the existence of a torqueing mechanism that leads to reduction in normal stress near the free surface for thrust earthquakes.

Data Availability Statement

The experimental data used for this study can be found at https://osf.io/nts3e.

References

Abrahamson, N. A., & Somerville, P. G. (1996). Effects of the hanging wall and footwall on ground motions recorded during the Northridge earthquake. *Bulletin of the Seismological Society of America*, *86*(1B), S93–S99.

Aldam, M., Bar-Sinai, Y., Svetlizky, I., Brener, E. A., Fineberg, J., & Bouchbinder, E. (2016). Frictional sliding without geometrical reflection symmetry. *Physics Review X*, *6*(4), 41023. https://doi.org/10.1103/PhysRevX.6.041023

Allen, C. R., Brune, J. N., Cluff, L. S., & Barrows, A. G., Jr. (1998). Evidence for unusually strong near-field ground motion on the hanging wall of the San Fernando fault during the 1971 earthquake. *Seismological Research Letters*, *69*(6), 524–531.

Andrews, D. J. (1976). Rupture velocity of plane strain shear cracks. *Journal of Geophysical Research*, *81*(32), 5679. https://doi.org/10.1029/JB081i032p05679

Bai, Y. (2017). Comparison of strong ground motion recordings of the Lushan, China, earthquake of 20 April 2013 with the next generation attenuation (NGA)-west2 ground-motion models. *Bulletin of the Seismological Society of America*, *107*(4), 1724–1736.

Brune, J. N. (1996). Particle motions in a physical model of shallow angle thrust faulting. *Proceedings of the Indian Academy of Sciences Earth and Planetary Sciences*.

Buades, A., Coll, B., & Morel, J. (2006). The staircasing effect in neighborhood filters and its solution. *IEEE Transactions on Image Processing*, *15*(6), 1499–1505.

Buades, A., Coll, B., & Morel, J. (2008). Nonlocal image and movie denoising. *International Journal of Computer Vision*, *76*(2), 123–139. https://doi.org/10.1007/s11263-007-0052-1

Burridge, R. (1973). Admissible speeds for plane-strain self-similar shear cracks with friction but lacking cohesion. *Geophysical Journal International*, *35*(4), 439–455.

Chang, T.-Y., Cotton, F., Tsai, Y.-B., & Angelier, J. (2004). Quantification of hanging-wall effects on ground motion: Some insights from the 1999 chi-chi earthquake. *Bulletin of the Seismological Society of America*, *94*(6), 2186–2197.

Donahue, J. L., & Abrahamson, N. A. (2014). Simulation-based hanging wall effects. *Earthquake Spectra*, *30*(3), 1269–1284.

Duan, B., & Oglesby, D. D. (2005). The dynamics of thrust and normal faults over multiple earthquake cycles: Effects of dipping fault geometry. *Bulletin of the Seismological Society of America*, *95*(5), 1623–1636.

Dunham, E. M., & Archuleta, R. J. (2004). Evidence for a supershear transient during the 2002 Denali fault earthquake. *Bulletin of the Seismological Society of America*, *94*(6B), S256–S268. https://doi.org/10.1785/0120040616

Dunham, E. M., & Bhat, H. S. (2008). Attenuation of radiated ground motion and stresses from three-dimensional supershear ruptures. *Journal of Geophysical Research*, *113*(B8).

Freund, L. B. (1979). The mechanics of dynamic shear crack propagation. *Journal of Geophysical Research*, *84*(B5), 2199–2209. https://doi.org/10.1029/JB084iB05p02199

Fujiwara, T., Kodaira, S., No, T., Kaiho, Y., Takahashi, N., & Kaneda, Y. (2011). The 2011 Tohoku-Oki earthquake: Displacement reaching the trench Axis. *Science*, *334*(6060), 1240. https://doi.org/10.1126/science.1211554

Gabuchian, V., Rosakis, A. J., Bhat, H. S., Madariaga, R., & Kanamori, H. (2017). Experimental evidence that thrust earthquake ruptures might open faults. *Nature*, *545*(7654), 336–339. https://doi.org/10.1038/nature22045

Gabuchian, V., Rosakis, A. J., Lapusta, N., & Oglesby, D. D. (2014). Experimental investigation of strong ground motion due to thrust fault earthquakes. *Journal of Geophysical Research: Solid Earth*, *119*(2), 1316–1336.

Gori, M., Rubino, V., Rosakis, A. J., & Lapusta, N. (2018). Pressure shock fronts formed by ultra-fast shear cracks in viscoelastic materials. *Nature Communications*, *9*(1), 4754. https://doi.org/10.1038/s41467-018-07139-4

Ide, S., & Takeo, M. (1997). Determination of constitutive relations of fault slip based on seismic wave analysis. *Journal of Geophysical Research*, *102*(B12), 27379–27391. https://doi.org/10.1029/97JB02675

Kanamori, H., & Brodsky, E. E. (2004). The physics of earthquakes. *Reports on Progress in Physics*, *67*(8), 1429.

Kozdon, J. E., & Dunham, E. M. (2013). Rupture to the trench: Dynamic rupture simulations of the 11 march 2011 Tohoku earthquake. *Bulletin of the Seismological Society of America*, *103*(2 B), 1275–1289. https://doi.org/10.1785/0120120136

Lay, T., Ammon, C. J., Kanamori, H., Xue, L., & Kim, M. J. (2011). Possible large near-trench slip during the 2011Mw 9.0 off the Pacific coast of Tohoku earthquake. *Earth Planets and Space*, *63*(7), 687–692. https://doi.org/10.5047/eps.2011.05.033

Li, X. J., Liu, L., Wang, Y. S., & Yu, T. (2010). Analysis of horizontal strong-motion attenuation in the great 2008 Wenchuan earthquake. *Bulletin of the Seismological Society of America*, *100*(5B), 2440–2449.

Linker, M. F., & Dieterich, J. H. (1992). Effects of variable normal stress on rock friction: Observations and constitutive equations. *Journal of Geophysical Research*, *97*(B4), 4923. https://doi.org/10.1029/92JB00017

Liu, Q., & Li, X. (2009). Preliminary analysis of the hanging wall effect and velocity pulse of the 5.12 Wenchuan earthquake. *Earthquake Engineering and Engineering Vibration*, *8*(2), 165–177.

Liu, Y., & Lapusta, N. (2008). Transition of mode II cracks from sub-rayleigh to intersonic speeds in the presence of favorable heterogeneity. *Journal of the Mechanics and Physics of Solids*, *56*(1), 25–50. https://doi.org/10.1016/j.jmps.2007.06.005

Lu, X., Rosakis, A. J., & Lapusta, N. (2010). Rupture modes in laboratory earthquakes: Effect of fault prestress and nucleation conditions. *Journal of Geophysical Research*, *115*(B12), B12302. https://doi.org/10.1029/2009JB006833

Ma, K. F., Mori, J., Lee, S. J., & Yu, S. B. (2001). Spatial and temporal distribution of slip for the 1999 chi-chi, Taiwan, earthquake. *Bulletin of the Seismological Society of America*, *91*(5), 1069–1087. https://doi.org/10.1785/0120000728

Ma, S., & Beroza, G. C. (2008). Rupture dynamics on a bimaterial interface for dipping faults. *Bulletin of the Seismological Society of America*, *98*(4), 1642–1658. https://doi.org/10.1785/0120070201

Madariaga, R. (2003). Radiation from a finite reverse fault in a half space. *Pure and Applied Geophysics*, *160*(3–4), 555–577. https://doi.org/10.1007/PL00012550

Mello, M., Bhat, H. S., & Rosakis, A. J. (2016). Spatiotemporal properties of sub-rayleigh and supershear rupture velocity fields: Theory and experiments. *Journal of the Mechanics and Physics of Solids*, *93*, 153–181. https://doi.org/10.1016/j.jmps.2016.02.031

Mello, M., Bhat, H. S., Rosakis, A. J., & Kanamori, H. (2010). Identifying the unique ground motion signatures of supershear earthquakes: Theory and experiments. *Tectonophysics*, *493*(3–4), 297–326. https://doi.org/10.1016/j.tecto.2010.07.003

Mello, M., Bhat, H. S., Rosakis, A. J., & Kanamori, H. (2014). Reproducing the supershear portion of the 2002 Denali earthquake rupture in laboratory. *Earth and Planetary Science Letters*, *387*, 89–96. https://doi.org/10.1016/j.epsl.2013.11.030

Nason, R. (1973). Increased seismic shaking above a thrust fault. In N. A. Benfer, J. L. Coffman, & J. R. Bernick (Eds.), *San Fernando, California, earthquake of February 9, 1971: Geological and geophysical studies* (Vol. 3, pp. 123–126). US Department of Commerce, National Oceanic and Atmospheric Administration.

Nielsen, S. B. (1998). Free surface effects on the propagation of dynamic rupture. *Geophysical Research Letters*, *25*(1), 125–128. https://doi.org/10.1029/97GL03445

Oglesby, D. D., Archuleta, R. J., & Nielsen, S. B. (1998). Earthquakes on dipping faults: The effects of broken symmetry. *Science*, *280*(5366), 1055–1059. https://doi.org/10.1126/science.280.5366.1055

Oglesby, D. D., Archuleta, R. J., & Nielsen, S. B. (2000). Dynamics of dip-slip faulting: Explorations in two dimensions. *Journal of Geophysical Research*, *105*(B6), 13643–13653. https://doi.org/10.1029/2000JB900243

Oglesby, D. D., & Day, S. M. (2001). The effect of fault geometry on the 1999 Chi-Chi (Taiwan) earthquake. *Geophysical Research Letters*, *28*(9), 1831–1834. https://doi.org/10.1029/2000GL012043

Palmer, A. C., & Rice, J. R. (1973). The growth of slip surfaces in the progressive failure of over-consolidated clay. *Proceedings of the Royal Society of London*, *332*, 527–548. https://doi.org/10.1098/rspa.1983.0054

Prakash, V., & Clifton, R. J. (1993). Time resolved dynamic friction measurements in pressure-shear. *Experimental Techniques in the Dynamics of Deformable Solids*, *165*, 33–48.

Rice, J. R., Sammis, C. G., & Parsons, R. (2005). Off-fault secondary failure induced by a dynamic slip pulse. *Bulletin of the Seismological Society of America*, *95*(1), 109–134. https://doi.org/10.1785/0120030166

Rosakis, A. J. (2002). Intersonic shear cracks and fault ruptures. *Advances in Physics*, *51*(4), 1189–1257. https://doi.org/10.1080/00018730210122328

Rosakis, A. J., Rubino, V., & Lapusta, N. (2020). Recent milestones in unraveling the full-field structure of dynamic shear cracks and fault ruptures in real-time: From photoelasticity to ultrahigh-speed digital image correlation. *Journal of Applied Mechanics*, *87*(3). https://doi.org/10.1115/1.4045715

Rosakis, A. J., Samudrala, O., & Coker, D. (1999). Cracks faster than the shear wave speed. *Science*, *284*, 1337–1340.

Rosakis, A. J., Xia, K., Lykotrafitis, G., & Kanamori, H. (2007). Dynamic shear rupture in frictional interfaces: Speeds, directionality, and modes. *Treatise on Geophysics*, *4*, 153–192.

Rubino, V., Lapusta, N., Rosakis, A. J., Leprince, S., & Avouac, J. P. (2015). Static laboratory earthquake measurements with the digital image correlation method. *Experimental Mechanics*, *55*, 77–94. https://doi.org/10.1007/s11340-014-9893-z

Rubino, V., Rosakis, A. J., & Lapusta, N. (2017). Understanding dynamic friction through spontaneously evolving laboratory earthquakes. *Nature Communications*, *8*, 1–12. https://doi.org/10.1038/ncomms15991

Rubino, V., Rosakis, A. J., & Lapusta, N. (2019). *Full-field ultrahigh-speed quantification of dynamic shear ruptures using digital image correlation*. Experimental Mechanics.

Rubino, V., Rosakis, A. J., & Lapusta, N. (2020). Spatiotemporal properties of sub-rayleigh and supershear ruptures inferred from full-field dynamic imaging of laboratory experiments. *Journal of Geophysical Research*, *125*(2). https://doi.org/10.1029/2019JB018922

Saffer, D. M., & Marone, C. (2003). Comparison of smectite- and illite-rich gouge frictional properties: Application to the updip limit of the seismogenic zone along subduction megathrusts. *Earth and Planetary Science Letters*, *215*(1), 219–235. https://doi.org/10.1016/S0012-821X(03)00424-2

Samudrala, O., Huang, Y., & Rosakis, A. J. (2002). Subsonic and intersonic shear rupture of weak planes with a velocity weakening cohesive zone. *Journal of Geophysical Research*, *107*(B8), https://doi.org/10.1029/2001JB000460

Scala, A., Festa, G., Vilotte, J., Lorito, S., & Romano, F. (2019). Wave interaction of reverse-fault rupture with free surface: Numerical analysis of the dynamic effects and fault opening induced by symmetry breaking. *Journal of Geophysical Research: Solid Earth*, *124*(2), 1743–1758.

Shi, B., Anooshehpoor, A., Brune, J. N., & Zeng, Y. (1998). Dynamics of thrust faulting: 2D lattice model. *Bulletin of the Seismological Society of America*, *88*(6), 1484–1494.

Shin, T.-C., & Teng, T. (2001). An overview of the 1999 chi-chi, Taiwan, earthquake. *Bulletin of the Seismological Society of America*, *91*(5), 895–913. https://doi.org/10.1785/0120000738

Singh, R. P., & Parameswaran, V. (2003). An experimental investigation of dynamic crack propagation in a brittle material reinforced with a ductile layer. *Optics and Lasers in Engineering*, *40*(4), 289–306.

Steinbrugge, K. V., Schader, E. E., & Moran, D. F. (1975). Building damage in san Fernando valley. *Bulletin – California, Division of Mines and Geology*, *196*, 323–353.

Tal, Y., Rubino, V., Rosakis, A. J., & Lapusta, N. (2019). Enhanced digital image correlation analysis of ruptures with enforced traction continuity conditions across interfaces. *Applied Sciences*, *9*(8). https://doi.org/10.3390/app9081625

Tal, Y., Rubino, V., Rosakis, A. J., & Lapusta, N. (2020). Illuminating the physics of dynamic friction through laboratory earthquakes on thrust faults. *Proceedings of the National Academy of Sciences*, *117*(35), 21095–21100.

Xia, K., Rosakis, A. J., & Kanamori, H. (2004). Laboratory earthquakes: The sub-rayleigh – to – supershear. *Science*, *303*, 1859–1861. https://doi.org/10.1126/science.1094022

Yin, J., & Denolle, M. A. (2021). The Earth's surface controls the depth-dependent seismic radiation of megathrust earthquakes. *AGU Advances*, *2*(3), e2021AV000413. https://doi.org/10.1029/2021AV000413

Zhang, Y., Zhang, D., Li, X., Huang, B., Zheng, W., & Wang, Y. (2019). Fault structural control on earthquake strong ground motions: The 2008 wenchuan earthquake as an example. In *Earthquakes and multi-hazards around the pacific rim* (Vol. II, pp. 73–85). Springer.